POLITECNICO
MILANO 1863

POLITECNICO DI MILANO
School of Industrial and Information Engineering
Department of Aerospace Science and Technology

Master Thesis in Aeronautical Engineering

Mechanical characterization of titanium alloy Ti6Al4V and 316L stainless steel manufactured by SLM

Author:
Marco Scarpetta
883517

Supervisor:
Antonio Mattia Grande
Co-Supervisor:
Anis Hor

Academic Year 2020

Agli Scarpetta, ai Topazio, al Girdino

Contents

1 Abstract **8**

2 Mechanical characterization of the anisotropy of the titanium alloy Ti6Al4V manufactured by SLM **10**

2.1 Bibliography report 10
2.1.1 Introduction 10
2.1.2 Presentation of the Additive Manufacturing processes . . . 12
2.1.3 Microstructure and texture of the titanium alloy Ti6Al4V manufactured by additive manufacturing 15
2.1.4 Anisotropy of the mechanical properties of the titanium alloy Ti6Al4V manufactured by SLM 18
2.1.5 Conclusion 22
2.2 Experimental study 23
2.2.1 Introduction 23
2.2.2 Description of the samples 24
2.2.3 Uniaxial tensile tests 27
2.2.4 Shear tests 32
2.3 Results and discussion 37
2.3.1 Uniaxial tensile tests 37
2.3.2 Shear tests 40
2.4 Conclusion 45

3 Fatigue behavior of stainless steel 316L manufactured by SLM **46**

3.1 Bibliography report 46
3.2 Experimental study 50
3.2.1 Introduction 50
3.2.2 Description of the samples 50
3.2.3 Tensile fatigue tests 52
3.2.4 Torsional fatigue tests 55
3.2.5 Bending fatigue tests 57
3.3 Results and discussion 58
3.3.1 Tensile fatigue tests 58
3.3.2 Torsional fatigue tests 60
3.3.3 Bending fatigue tests 64
3.4 Conclusion 68

4 Conclusion and perspectives **69**

List of Figures

1 Examples of AM applications 8
2 Percentage of aluminum, titanium, and steel alloys and FRP of the structural weight of modern large commercial aircraft and gas turbine engines [2] 10
3 Some areas of titanium use in military and civil aeronautics [3] . . 11
4 Global sales of metal AM systems [8] 12
5 SLM process mechanics 13
6 Effect of laser on powder bed 14
7 Research publications on SLM of various materials [13] 14
8 Optical micrograph of an as-deposited component. The dark bands are attributed to the molten pools [19] 16
9 Microstructures of heat treated components [24] 18
10 Summary of relevant Ti–6Al–4V mechanical properties reported in literature - Elongation [24, 25, 26, 27, 30, 31, 32, 35] 19
11 Summary of relevant Ti–6Al–4V mechanical properties reported in literature - Strength [24, 25, 26, 27, 30, 31, 32, 35] 21
12 Tensile test configuration 23
13 Depiction of the tray, with the axes of manufacturing. Z_M, the construction direction, is out-of-plane. The cylindrical specimens are out of the scope of this project 24
14 Stress relieving heat treatment 26
15 Measurement systems 26
16 Specimen for uniaxial tensile test 27
17 VIC-3D® processing 29
18 Data visualization for vertical strain 30
19 Stress-strain curves obtained through different methods. The "Average" and the "Virtual SG" are coincident. The slipping of the strain gauge is evident in "SG" 30
20 Post-treatment process for tensile tests 31
21 Stress-strain diagram obtained for one of the specimens. The straight line has been drawn to identify the yield stress 31
22 Specimen for shear test 32
23 Shear strain 33
24 Post-treatment process for the shear tests 34
25 Shear specimen modelled on Abaqus FEA 35
26 Boundary conditions applied for the numerical model 35
27 Detail of the mesh in the shear zone 36
28 Visualization for the shear strain 36
29 Results from tensile tests - Average strength values for each orientation 38

30 Results from tensile tests - Average elongation values for each orientation . . . 38
31 Results from tensile tests - Stress-strain curves for a specimen for each orientation . . . 39
32 Results from shear tests - Stress-strain curves for a specimen for each orientation . . . 42
33 Results from shear and tensile tests - Average equivalent strength values for each orientation . . . 44
34 Results from shear and tensile tests - Average equivalent strain values for each orientation . . . 44
35 Summary of fatigue limits for 316L stainless steel for different heat and surface treatments reported in literature [53, 66, 67, 68] . . . 48
36 Representation of the three different surface finishes [68] . . . 49
37 Manufacturing of the SS316L specimens . . . 51
38 Stress relieving heat treatment . . . 51
39 Tensile specimen geometry . . . 52
40 Biaxial testing system used for the tensile tests . . . 52
41 Example of application of staircase method . . . 54
42 Torsion specimen geometry . . . 55
43 Testing machine used for torsional and bending tests . . . 55
44 Resonance frequency during a fatigue test . . . 56
45 Bending specimen geometry . . . 57
46 Wöhler diagram for tensile specimens . . . 60
47 Wöhler diagram for torsional specimens . . . 63
48 Wöhler diagram for bending specimens . . . 68

List of Tables

1 Summary of relevant Ti–6Al–4V mechanical properties reported in literature - Elongation . . . 19
2 Summary of relevant Ti–6Al–4V mechanical properties reported in literature - Strength . . . 21
3 Production parameters for the manufacturing of the Ti6Al4V specimens . . . 24
4 Labeling table for the available specimens. The cylindrical specimens were not used for this project . . . 25
5 Available tensile specimens . . . 27
6 Available shear specimens . . . 32
7 Results from tensile tests . . . 37
8 Results from tensile tests - Average values for each orientation . . . 37
9 Results from shear tests . . . 40
10 Results from shear tests - Average values for each orientation . . . 40
11 Results from shear tests - Equivalent stress, strain . . . 42
12 Results from shear and tensile tests - Average equivalent values for each orientation . . . 43
13 Summary of fatigue limits for 316L stainless steel for different heat and surface treatments reported in literature . . . 49
14 Production parameters for the manufacturing of the SS316L specimens . . . 50
15 Staircase method for as-built and polished tensile specimens . . . 58
16 Staircase method calculations for as-built and polished tensile specimens . . . 58
17 Summary of all the tensile fatigue tests conducted . . . 59
18 Staircase method for as-built, polished, machined and polished torsional specimens . . . 60
19 Staircase method calculations for as-built, polished, machined and polished torsional specimens . . . 61
20 Summary of all the torsional fatigue tests conducted . . . 63
21 Staircase method for as-built, polished, machined and polished bending specimens . . . 64
22 Staircase method calculations for as-built, polished, machined and polished bending specimens . . . 64
23 Staircase method for wrought, machined and polished bending specimens . . . 65
24 Staircase method calculations for wrought, machined and polished bending specimens . . . 65
25 Summary of all the bending fatigue tests conducted . . . 67
26 LCF tests on wrought, machined and polished bending specimens 67

1 Abstract

The term "Additive Manufacturing" (AM) references technologies that grow three dimensional objects one superfine layer at a time [4]. Each successive layer bonds to the preceding one of melted or partially melted material.
With AM techniques, it is possible to obtain near net shape parts with quite fine resolution.
Selection of the right AM technology along with proper design optimization can lead to very significant savings through reduction of buy-to-fly ratios, overall weight and scrap.
AM applications are limitless: from pre-production visualization models to the fabrication of end-use products in different fields, as shown in figure 1.

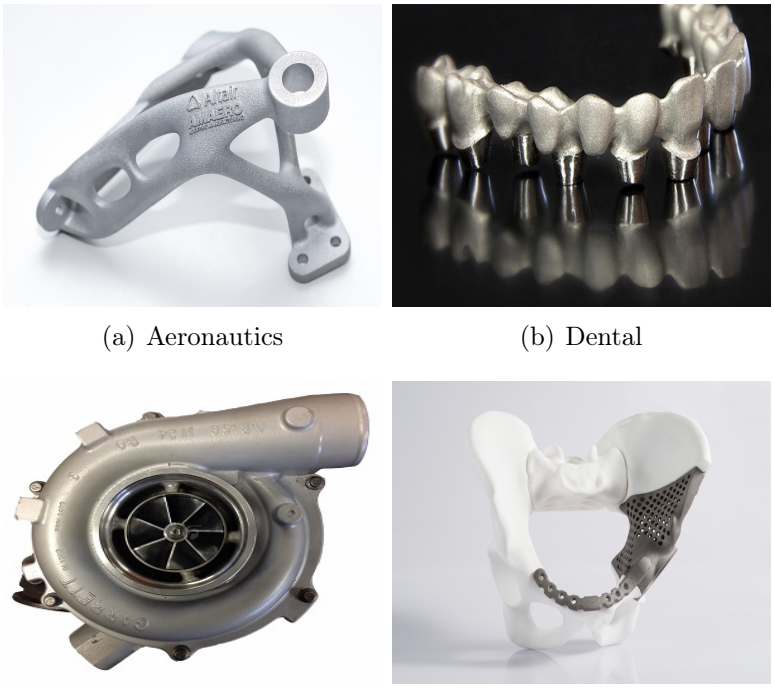

(a) Aeronautics (b) Dental

(c) Automobiles (d) Medicine

Figure 1: *Examples of AM applications*

However, the efforts currently underway to develop AM methods will not avoid the question of anisotropy [5]: indeed, this kind of unidirectional manufacture will in all probability exacerbate it [6].
Moreover, the presence of defects of different natures in the AM products can significantly influence the fatigue resistance, providing micro-cracks that can propagate and cause the failure of the part.
For this project, two analysis have been performed: one on the mechanical anisotropy of Ti6Al4V (grade 5), conducting tensile and shear tests on samples manufactured

by SLM technique, along different build directions, and one on the fatigue behavior of SS316L, conducting cyclic tests in traction, torsion and bending on samples manufactured by SLM technique, subject to different surface treatments.
The first analysis, on the Ti6Al4V pieces, has shown as expected an anisotropic behavior, with the best results in terms of ductility and strength obtained for specimens with build direction parallel to the direction of the principal stresses.
The second analysis, on the SS316L pieces, has shown an improvement in fatigue resistance for polished specimens, and a further improvement for machined and polished specimens in comparison to the ones without surface treatment. However, the fatigue limit obtained for every SLM piece has proven to be lower than the reference limit for wrought samples.

2 Mechanical characterization of the anisotropy of the titanium alloy Ti6Al4V manufactured by SLM

2.1 Bibliography report

2.1.1 Introduction

Titanium alloys are amongst the most important of the advanced materials which are key to improved performance in aerospace and terrestrial system. This is because of the excellent combinations of specific mechanical properties and outstanding corrosion behavior exhibited by titanium alloy, as well as a good heat resistance [1, 2]. In particular, Ti6Al4V, the "workhorse alloy of titanium industry", captures a large portion of aerospace applications today, as shown in figures 2, 3, as its uses span many aerospace airframe (like general structural material, bolts, seat rails) and engine (fan blades, fan case) component uses, and also major non aerospace applications in the marine, offshore and power generation industries in particular [3].
However, negating widespread use is the high cost of titanium alloys compared to competing materials.

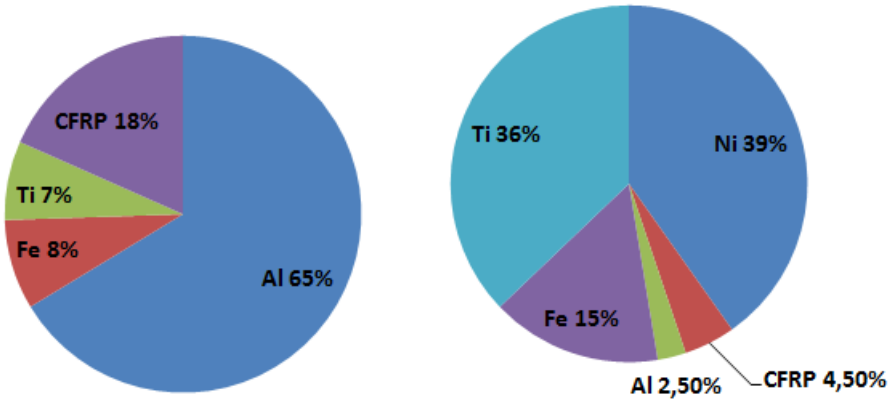

(a) Structural weight (b) Gas turbine engines

Figure 2: *Percentage of aluminum, titanium, and steel alloys and FRP of the structural weight of modern large commercial aircraft and gas turbine engines [2]*

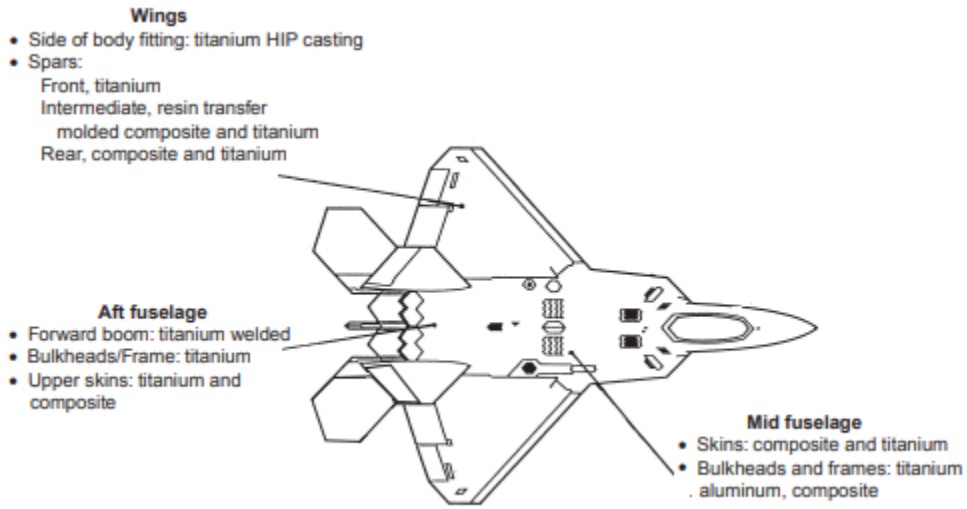

(a) F-22 airframe

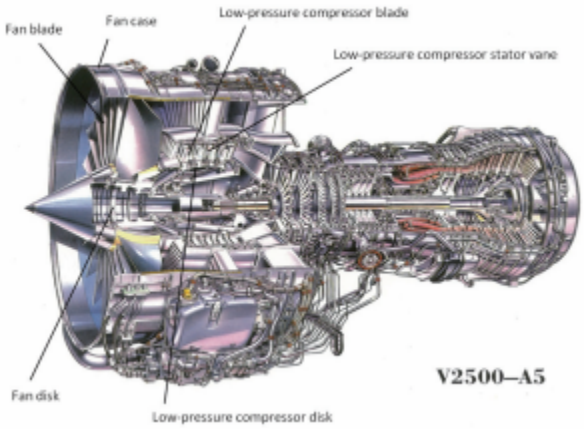

(b) IAE V2500 engine

Figure 3: *Some areas of titanium use in military and civil aeronautics [3]*

2.1.2 Presentation of the Additive Manufacturing processes

Additive Manufacturing is a process of making a three-dimensional solid object of virtually any shape from a digital model. It is achieved using an additive process, where successive layers of material are laid down in different shapes. The ASTM Committee F42 on Additive Manufacturing Technologies publishes the official terminology standard for the industry. ASTM F2792-12a [7] generically defines seven process classifications for Additive Manufacturing, specifically:

- Binder Jetting;
- Directed Energy Deposition;
- Material Extrusion;
- Material Jetting;
- Powder Bed Fusion;
- Sheet Lamination;
- Vat Photopolymerization.

In these years there has been an exponential growth of the interest on the AM applications for metals [8] in the fields of research and industry, as shown in figure 4, and the most popular techniques for AM of metals have turned out to be Selective Laser Melting (SLM), Electron Beam Melting (EBM), both classified as Powder Bed Fusion processes, and Laser Metal Deposition (LMD), classified as a Direct Energy Deposition process [9].

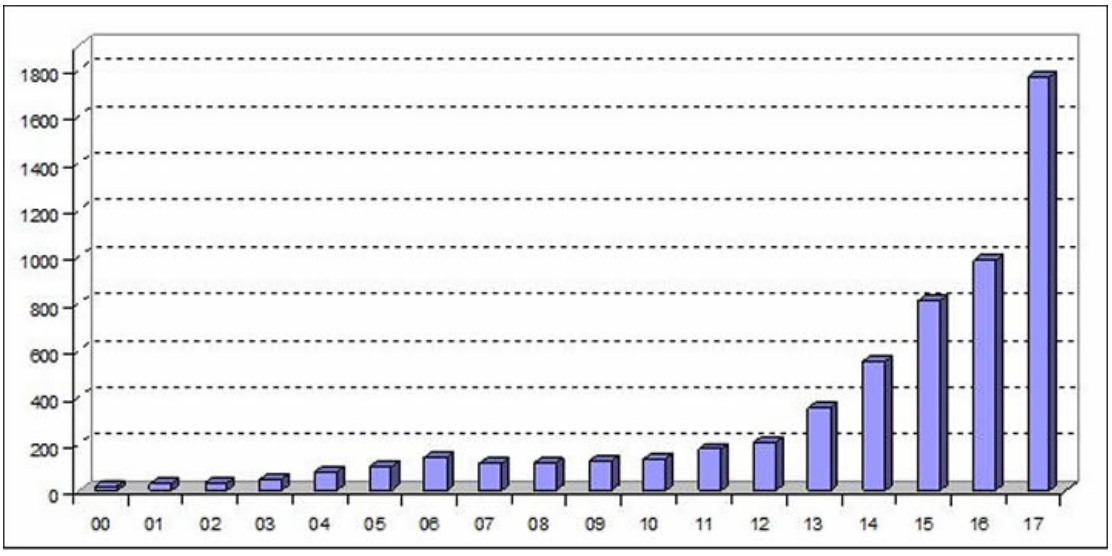

Figure 4: *Global sales of metal AM systems [8]*

In particular, the samples tested for this project have been manufactured with the Selective Laser Melting (SLM) technique. With this technique, a high energy density laser is used to melt and fuse metallic parts together, in an inert gas atmosphere. Since the powder is fully melted, it is possible to have low porosity and a good control over crystal structure, acting on the production parameters (such as laser power, scanning speed, hatch spacing, and layer thickness).
This process was invented at the Fraunhofer Institute ILT in Aachen, Germany, in 1996 [10], and was initially classified as "laser sintering" technique. Nevertheless, there is a significant difference between SLM and SLS (Selective Laser Sintering): while the first fully melts the powder, the second heats it up to a specific point where the powder grains can fuse together; thus, SLS cannot achieve the near full density which characterizes the SLM products, and furthermore it usually requires postprocessing, such as heat treatment and material infiltration.
The SLM building process starts with laying a thin layer of metal powder on a substrate plate in a building chamber. After the powder is laid, the laser is used to melt and fuse selected areas according to the processed data. Once the laser scanning is completed, the building platform is lowered, a next layer of powder is deposited on top and the laser scans a new layer. The process is then repeated for successive layers of powder until the required components are completely built. The process is represented in figures 5, 6.

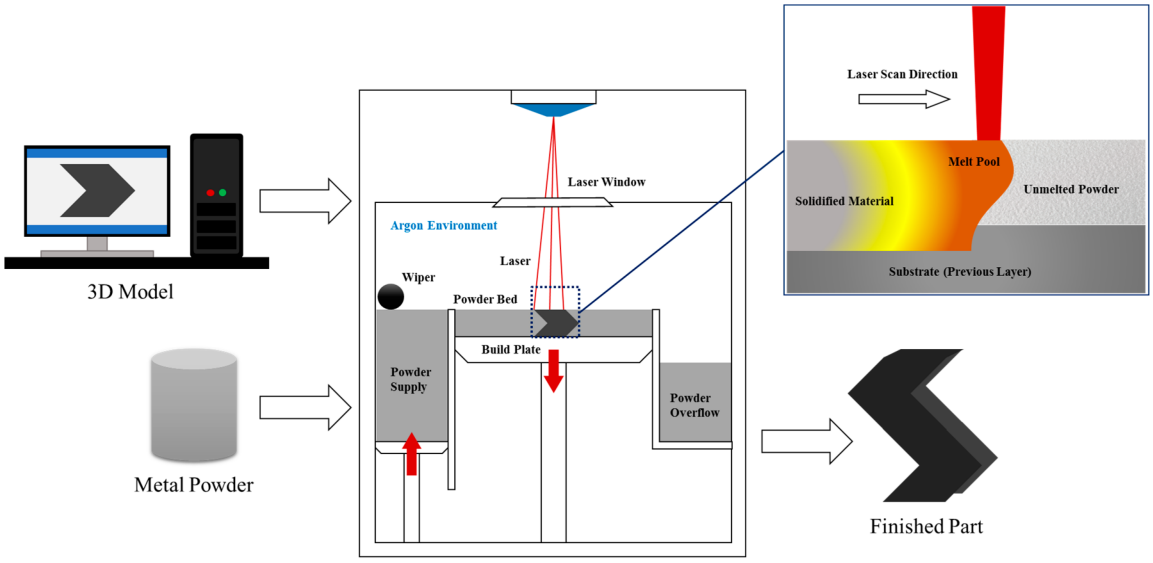

Figure 5: *SLM process mechanics*

There are several physical phenomena that have to be taken into account, such as the absorption of laser irradiation by the powder material, the balling phenomena, that disrupt the formation of continuous melts, or the thermal fluctuation experienced by the material during the process, that causes residual stress on the components built, and can therefore lead to crack formation and delamination.

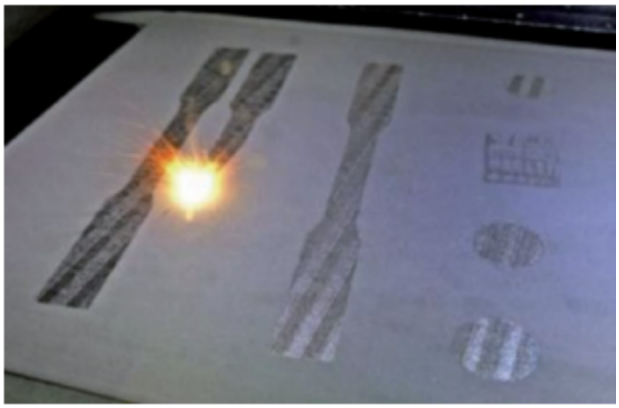

Figure 6: *Effect of laser on powder bed*

The question of residual stress in particular has received a great deal of attention, since it can generate part distortion, and thus a dramatic functionality deterioration [11]. It was found that, for a chrome molybdenum steel powder mixed with copper phosphate and nickel powders, a heat treatment at 600 ℃–700 ℃ for an hour reduced residual stress by 70%, re-scanning of laser with the same parameters as the SLM forming process reduced residual stress by 55%, and heating of powder bed to 160 ℃ resulted in a 40% reduction [12].
A literature survey [13] has shown that more than half of all the publications on SLM from 1999 to 2014 concerned steel and titanium, especially 316L stainless steel and Ti6Al4V alloy, as displayed in figure 7.

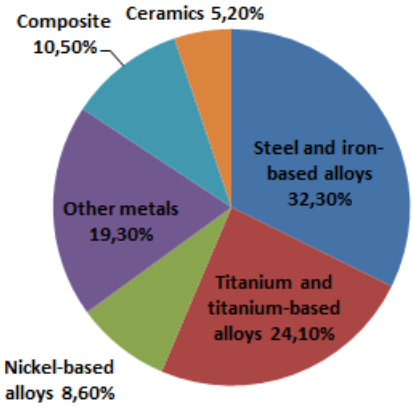

Figure 7: *Research publications on SLM of various materials [13]*

Regarding titanium, SLM has been proven to be suitable to the material, since for this process an inert gas, such as argon, is used to flush out atmospheric air and provide a layer of protective gas from elements such as oxygen, nitrogen, hydrogen, and carbon, to which the metal is highly reactive and sensitive, making it difficult for conventional processes.

Moreover, small localized heating and rapid cooling in SLM reduce the pick-up of interstitial elements. Previous studies have shown good results in terms of relative density, especially under high laser power and low scanning speed [14], and strength (UTS, YS) of the manufactured pieces, compared to parts produced by casting or other AM techniques [15].

2.1.3 Microstructure and texture of the titanium alloy Ti6Al4V manufactured by additive manufacturing

In order to analyze the anisotropy of the alloy Ti6Al4V it is necessary to observe the microstructure and the texture, since they can have a profound influence on the mechanical behavior.
This alloy is a two phase $\alpha + \beta$, with aluminum as the alpha stabilizer and vanadium as the beta stabilizer. Aluminum and vanadium also reduce the density and raise the high-temperature ductility; the material shows therefore a positive response to heat treatments, a good stability under strain and a low resistance to metal forming processes.
For this study, the analyzed specimens were made of Ti6Al4V grade 5, the most commonly used of the titanium alloys. Its chemical composition consists of [16]:

- Nitrogen (maximum weight: 0.05%)
- Carbon (maximum weight: 0.1%)
- Hydrogen (maximum weight: 0.0125%)
- Oxygen (maximum weight: 0.2%)
- Iron (maximum weight: 0.3%)
- Aluminum (maximum weight: 6.75%; minimum weight: 5.5%)
- Vanadium (maximum weight: 4.5%; minimum weight: 3.5%)
- Titanium (balance)

It has been stated that, since SLM materials solidify with high cooling rates, there is the formation of a metastable structure; in the case of Ti6Al4V, the microstructure typically consists of α' martensite [17].
The solidification starts in this case from crystallization of cubic β phase from the liquid. Commonly, cubic phase is crystallized with a preferential crystallographic direction <100>. Further cooling leads to a transformation of β phase to α' at high cooling rates (SLM), or $\alpha + \beta$ at lower cooling rates (EBM). In both cases, there is a relationship between the crystallographic orientation of the hexagonal α phase with that of the parental β.

It is suggested that when the laser hits the powder bed, the grains in the previous deposited layers and the powder particles of the top layer transform into the β phase field [18]. The β grains then solidify and grow epitaxially along the direction of heat conduction (typically in a columnar way in the build direction), since there is no nucleation barrier to solidification. Therefore, the orientation of these grains is highly dependent on the scanning velocity and scanning strategy. Finally, as the laser moves away across the powder bed multiple α' martensitic laths precipitate within the elongated columnar grain of the parent β grain.
Thus, the microstructure of the components is composed of fine acicular α' grains throughout the sample and only prior β grain boundaries are left behind after the solidification. The presence of prior β columnar grain boundaries is due to the fact that Ti-6Al-4V solidifies in the β phase field and heat is mainly conducted away vertically. Prior β grains have a lenticular morphology with an high aspect ratio, as shown in figure 8.

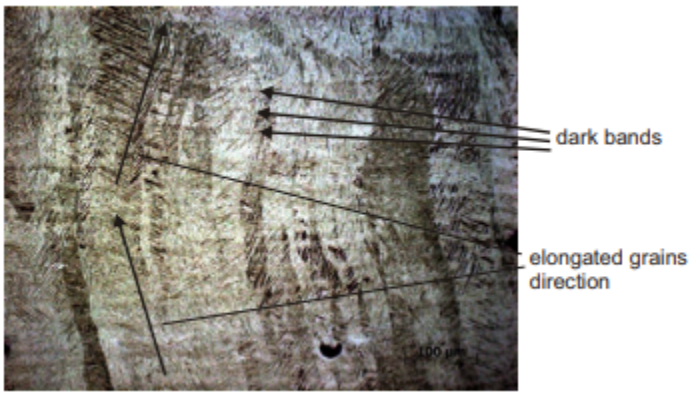

Figure 8: *Optical micrograph of an as-deposited component. The dark bands are attributed to the molten pools [19]*

Instead, α' grains do not vary in size along the build and scanning directions. The α' martensitic laths are organized within prior β grain boundaries with different inclinations, mainly at $\pm 45°$ and $90°$ to the build direction. The α' grains do not precipitate along the β grain boundaries, and this suggests that the α' grains originate simultaneously from different points within the parent β grain which is typical of martensitic transformations. The α' phase appeared as relatively long and narrow laths characterized by high vanadium content and high dislocation density. The overall α' texture appears random because of the relatively high number of α' variants within each prior β grain, i.e. the large number of micron sized α' grains that precipitate within the columnar β grains, which grow in multiple directions and random orientation. These variants precipitate in clusters forming boundary misorientations that minimize the strain energy associated with martensitic transformation.

During the deposition of successive layers texture inheritance seems to occur within prior β grains. Moreover, α' grains of similar inclination have the same crystal orientation. Although variant selection at prior β grain boundaries is unlikely due to the fast cooling that occurs during SLM it is possible that certain variants might be chosen among others to minimize the phase transformation energy.
Furthermore, it was observed that the fast solidification during the SLM process leads to segregation of aluminum. When a relatively amount of heat is applied to the material, i.e. the parameters hatch spacing and scanning velocity are set to low values, precipitation of an intermetallic Ti_3Al phase occurs [19].
Previous studies have remarked that, while the presence of a fine-grained microstructure can improve the yield and tensile strengths, the tensile elongation values at rupture for AM components (6%-11%) are lower than those observed in wrought conditions (12%-17%) [20]. This can be possibly attributed to several reasons: the presence and cracking of grain boundary hexagonal close-packed (hcp) α-phase [21], the fine-grained microstructure [22], and the presence of titanium martensite [23].
The effects of heat treatments have also been investigated [24]: when the material is treated above the β transus temperature, the typical structure with fine acicular martensite and prior columnar grains is erased: during heating, the SLM material gradually transforms back to the original columnar β grains. However, these columnar grains are no longer present after cooling from above the β transus. Instead, the microstructure consists of α colonies inside large, semi-equiaxed, previous β grains. Therefore, a Widmanstätten structure is formed for intermediate cooling rates between air cooling and furnace cooling, and the α phase is present as flat plates or needles.
It was remarked that heat treatments at temperatures above the β transus cause extensive grain growth, up to the point where the columnar grains resemble a coarse equiaxed microstructure with large grains.
Instead, for heat treatments at temperatures below the β transus, the mixture of α and β phase prevents grain growth and the original, columnar prior β grains remain visible after cooling. The two different microstructures are displayed in figure 9.
The optimal results for tensile properties have been obtained for heat treating at intermediate to high temperatures below the β transus, followed by furnace cooling, with deformability levels safely above the prescribed standards and yield stress and UTS levels close to 1 GPa.

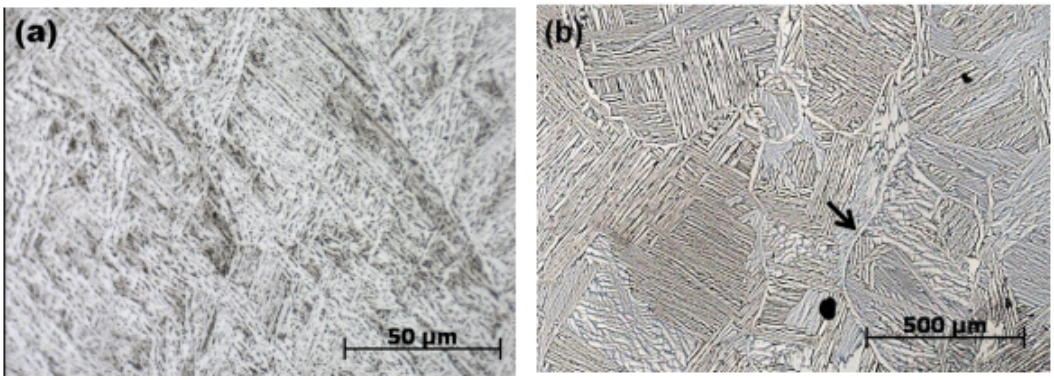

(a) Component after heat treatment below β transus temperature, followed by furnace cooling

(b) Component after heat treatment above β transus temperature, followed by furnace cooling. The arrows indicate grain boundary α

Figure 9: *Microstructures of heat treated components [24]*

2.1.4 Anisotropy of the mechanical properties of the titanium alloy Ti6Al4V manufactured by SLM

The unidirectionality, one of the defining characteristics of every AM process, induces an anisotropic microstructure in the produced components. Therefore, it is necessary to investigate how the anisotropy in the microstructure can influence the mechanic behavior of SLM products.
In general, it was observed that the the tensile strengths of SLMed Ti-6Al-4V samples are superior to those of the as-cast and wrought ones, while the elongations of SLMed Ti-6Al-4V samples are fairly lower, compared with the as-cast or wrought ones [16]. The better performances in terms of yield stress and UTS were attributed to the martensitic microstructure [25, 26], while the worsening in ductility was ascribed to porosity, as well as to the martensitic microstructure: as the α' grains do not form colonies of laths sharing the same orientation, the effective slip length is confined to single grains. [27, 38].
In fact, it was remarked that a heat treatment, able to reduce the lack-of-fusion defects [28] and to change the microstructure, from the martensitic one to a biphasic one, with columnar α-phase crystals formed at the boundaries of the original martensitic plates and an α-β mixture within [27], significantly increased the ductility (from around 8% to around 11%).
Previous studies were plagued by two types of pores: round gas entrapment pores and lack-of-fusion pores in which the melted metal in one layer did not completely fill the gaps between material passes in previous layers, resulting in thin flat cracks perpendicular to the build direction [29].

The sharp angles in lack-of-fusion pores result in local stress concentrations during loading; thus, these pores have been shown to play a significant role in early fracture, particularly in the transverse direction.
A review of existing articles [30] has proven that, in general, the specimens are more ductile in longitudinal direction than in the transverse one, as shown in table 1 and figure 10. It was hypothesized that this tendency is strongly influenced by the lack-of-fusion pores, existing between the layers.

Reference	Tensile axis orientation	Elongation (%)
[31]	Longitudinal	6.5±0.6
[27]	Longitudinal	8.2±0.3
[26]	Longitudinal	7.6±2
[26]	Transverse	1.7±0.3
[24]	Longitudinal	7.3±1.1
[32]	Transverse	1.6
[25]	Longitudinal	5±0.5
[25]	Transverse	4.89±0.6
[30]	Longitudinal	13.3±1.8
[30]	Transverse	18.7±1.7
[35]	Longitudinal	7
[35]	Transverse	24

Table 1: *Summary of relevant Ti–6Al–4V mechanical properties reported in literature - Elongation*

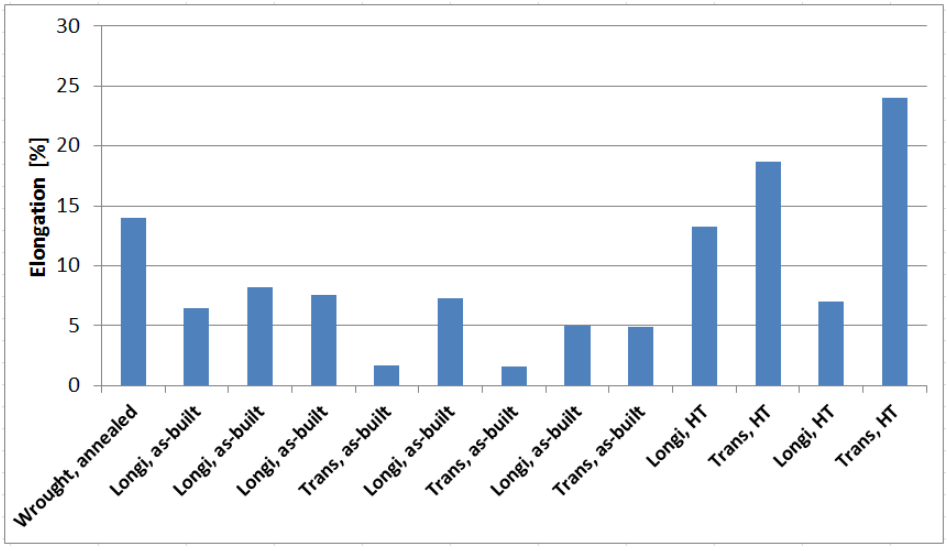

Figure 10: *Summary of relevant Ti–6Al–4V mechanical properties reported in literature - Elongation [24, 25, 26, 27, 30, 31, 32, 35]*

However, when a heat treatment was applied, and therefore the porosity was greatly reduced, the elongation was increased; in particular, it was observed that the ductility in the transverse direction was greater than that in the longitudinal direction [30, 35, 37].
This was related to the anisotropic microstructure: in fact, it is well documented that the presence of grain boundary α phase tends to reduce elongation in conventionally processed Ti–6Al–4V by furnishing a preferential path for damage accumulation along the prior-β grain boundaries [33]. Tensile loads perpendicular to the grain boundary act to separate adjacent prior-β grains. Therefore, the morphology of the prior-β grains in the SLM component results in different amounts of the grain boundary α phase being exposed to a tensile opening mode depending on whether tension is applied along the longitudinal or transverse direction.
In specimens in which tension is applied along the transverse direction, only the short axes of the prior-β grain boundaries and grain boundary α are subjected to Mode I opening tension.
Conversely, in specimens where tension is applied in the longitudinal direction, the long axes of the prior-β grains are loaded in tension, causing the entire length of the grain boundary α phase to be subjected to Mode I opening tension.
Thus, the anisotropic microstructure predisposes the longitudinal specimens to Mode I opening failure along the prior-β grain boundaries, but not the transverse specimens. The reduced elongation of the longitudinal specimens compared with the transverse may be a result of discontinuous grain boundary α phase and the presence of the preferentially oriented prior-β grain boundaries [34, 36].
Anisotropy was observed also for yield stress and UTS: in general, both these quantities are greater for specimens tested along the longitudinal direction with respect to the specimens tested along the transverse direction, even if in a less significant when compared to the elongation, as shown in table 2 and figure 11.

Reference	Tensile axis orientation	yield stress (MPa)	UTS (MPa)
[31]	Longitudinal	1100±12	1211±31
[27]	Longitudinal	1040±10	1140±10
[26]	Longitudinal	1137±20	1206±8
[26]	Transverse	962±47	1166±25
[24]	Longitudinal	1110±9	1267±5
[32]	Transverse	1008	1080
[25]	Longitudinal	1195±19	1269±9
[25]	Transverse	1143±30	1219±20
[30]	Longitudinal	960±26	1063±20
[30]	Transverse	945±13	1041±12
[35]	Longitudinal	1037	1181
[35]	Transverse	1000	1182

Table 2: *Summary of relevant Ti–6Al–4V mechanical properties reported in literature - Strength*

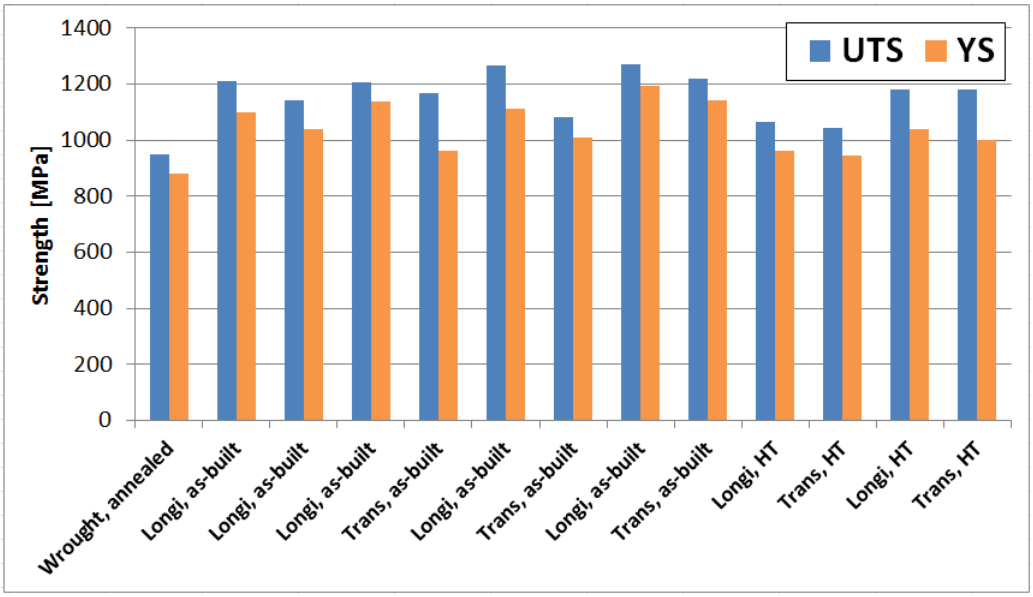

Figure 11: *Summary of relevant Ti–6Al–4V mechanical properties reported in literature - Strength [24, 25, 26, 27, 30, 31, 32, 35]*

The α' phase present in the coupons contributes to the yield stress anisotropy since α titanium is plastically anisotropic [39].
The orientation of the grains to a preferred slip system will promote dislocation movement; therefore, the mechanical properties are dependent on the crystallographic direction. Longitudinally built coupons have been shown to contain a larger number of grains in a stress state which are easier to slip than transverse coupons [37].

Another important contribution to the strength anisotropy derives from the presence of the defects, depending on their orientation with respect to the loading direction [40].
Finally, it is also possible that the difference in yield stress and ductility can be explained with respect to the combination of varying volumes of coarse and ultrafine α' martensite. The grain size can have a significant influence on the yield stress of Ti-6Al-4V, where ultrafine grained Ti-6Al-4V can have much higher yield stress than a coarser grained version of the same phase distribution. Therefore, slight variations in yield stress can occur with alterations in the volume fraction of ultrafine α'. The increased yield stress with grain refinement is typically associated with the loss of ductility [41, 42].

2.1.5 Conclusion

AM techniques are rapidly developing in these years, as they can bring benefits in terms of weight and scrap reduction. SLM is one of the most considered AM processes, and a large part of SLM products is in the titanium alloy Ti6Al4V, the "workhorse alloy of titanium industry".
However, as SLM produces components with an anisotropic microstructure, consisting of prior β columnar grains and fine acicular α' grains, it is important to analyze the anisotropy of the mechanical behavior of SLMed Ti6Al4V specimens. A dependency on orientation was observed for yield stress and UTS, and, to a greater extent, for the ductility. This was attributed to the microstructure and to the presence of defects typical of the process, especially lack-of-fusion pores.
When these defects are dominant, the elongation at failure for the specimens tested along the build direction is greater than that for the specimens tested perpendicularly to the build direction; instead, when these defects are eliminated through a heat treatment or through the optimization of the process parameters, the ductility is greatly increased, and the best results are observed in case of transverse tensile axis orientation.
The anisotropy for yield stress is less evident, yet not negligible; the tendency is opposite to the one for the elongation at rupture: the increased strength is typically associated with the loss of ductility. Therefore, the best results are obtained in the case of longitudinal tensile axis orientation.

2.2 Experimental study

2.2.1 Introduction

The purpose of this study is to analyze the anisotropy of the mechanical behavior of Ti6Al4V produced by SLM. To do this, tensile tests were conducted on two types of specimens, each of them manufactured along different orientations (0°, 30°, 45°, 60°, 90°) with respect to the perpendicular to the horizontal build plate, using a high capacity testing system for tensile, compression and flexure tests: Instron® 5900 R, shown in figure 12.
In order to measure displacements and strains, a method of digital image correlation was employed, using in particular the VIC-3D® measurement system, which provides Lagrange strains.

(a) Experimental set-up (b) Detail on the specimen fixing

Figure 12: *Tensile test configuration*

2.2.2 Description of the samples

For this study two types of flat samples have been used: standard specimen for the uniaxial tensile tests, and modified simple shear specimen based on the ASTM standard B831 [43].
The used production parameters are shown in table 3.

Labeling rate	1800 mm/s
Slew rate	5000 mm/s
Laser power	300 W
Spacing	50 μm
Strategy	Hexagonal (island pattern)
Overlap between hexagons	100 μm
Laser spot size	70 μm

Table 3: *Production parameters for the manufacturing of the Ti6Al4V specimens*

16 specimens of each type were manufactured, for a total of 32 pieces, as specified in figure 13 and table 4.

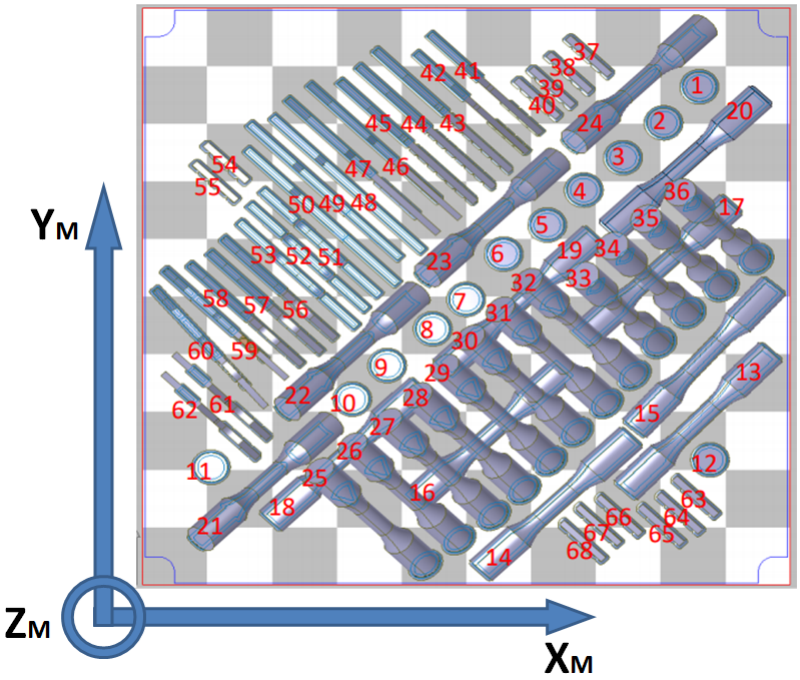

Figure 13: *Depiction of the tray, with the axes of manufacturing. Z_M, the construction direction, is out-of-plane. The cylindrical specimens are out of the scope of this project*

Identification number	Specimen type
1-2-3-4-5-6-7-8-9-10-11-12	Cylindrical 0°
37-38-39-40-54-55	Tensile 0°
63-64-65-66-67-68	Shear 0°
13-14-15-16-17-18-19-20	Cylindrical 90°
51-52-53	Tensile 90°
48-49-50	Shear 90°
25-26-27-28-29-30-31-32	Cylindrical 45°
56-57-58	Tensile 45°
43-44-45	Shear 45°
21-22-23-24	Cylindrical 60°
59-60	Tensile 60°
46-47	Shear 60°
33-34-35-36	Cylindrical 30°
61-62	Tensile 30°
41-42	Shear 30°

Table 4: *Labeling table for the available specimens. The cylindrical specimens were not used for this project*

The samples have been subjected to a stress relieving heat treatment, shown in figure 14.
It consisted of heating at a temperature which is high enough to greatly reduce the residual stress, but not enough to change the microstructure obtained through the manufacturing (in this case 720℃, below the β transus temperature), holding the temperature for a sufficient time (in this case about two and a half hours), and finally slowly cooling to room temperature. A slow cooling speed is important to avoid tensions caused by temperature differences in the material.
This treatment was performed in a furnace, in a protective atmosphere.
The surfaces of the specimens were spray-painted, as displayed in figure 15, in order to obtain little black dots on a white background; in this way the software of digital image correlation could correctly extrapolate the displacements and strains. The same data was measured using a strain gauge.

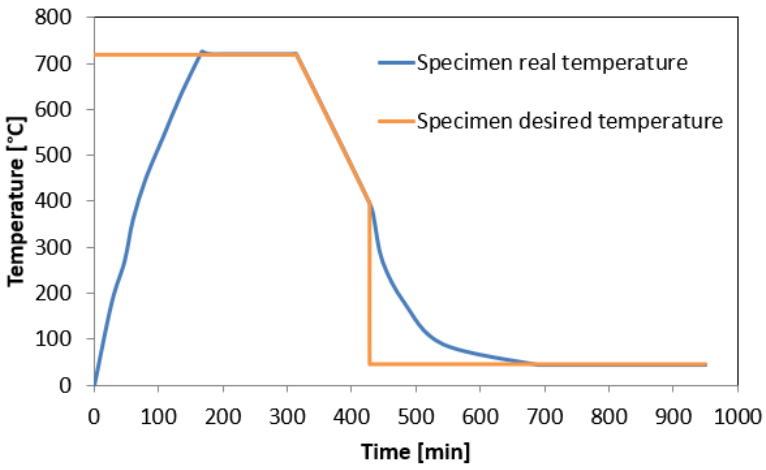

Figure 14: *Stress relieving heat treatment*

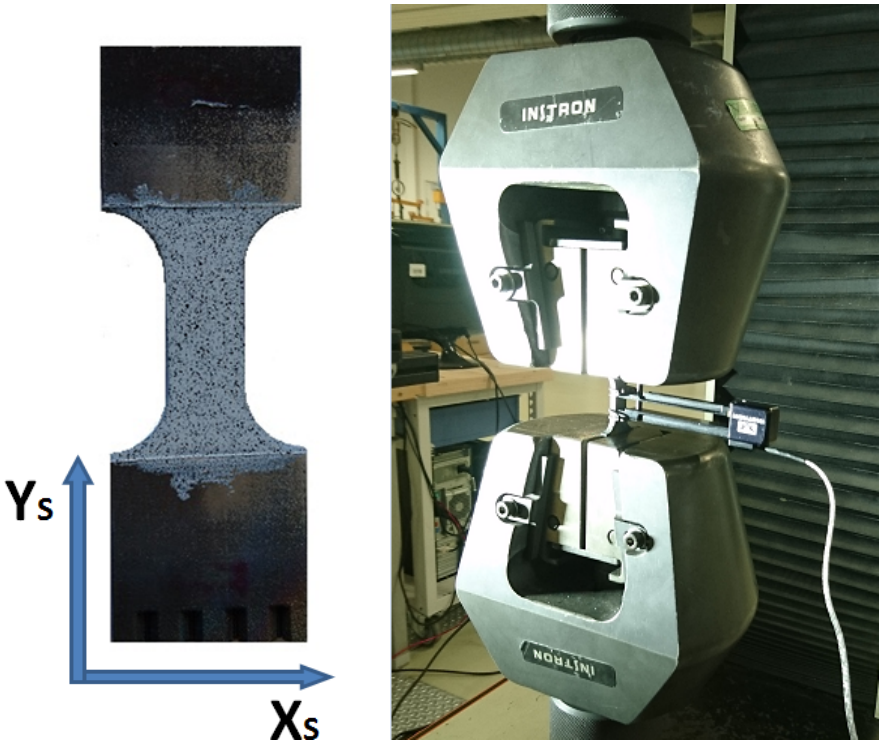

(a) Spray-painted specimen (b) Strain gauge

Figure 15: *Measurement systems*

2.2.3 Uniaxial tensile tests

The available specimens for the uniaxial tensile tests were 16, as specified in table 5. Their geometry is diplayed in figure 16.

Identification number	Orientation (°)
37-38-39-40-54-55	0
61-62	30
56-57-58	45
59-60	60
51-52-53	90

Table 5: *Available tensile specimens*

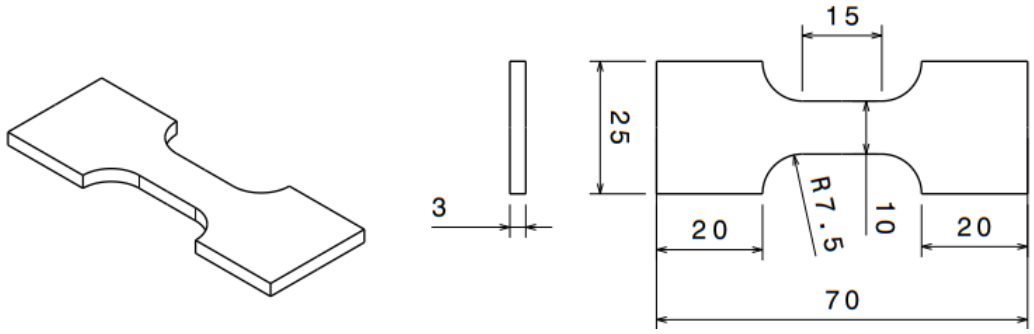

(a) Isometric view (b) Specimen geometry

Figure 16: *Specimen for uniaxial tensile test*

These angles are taken with respect to the vertical direction, perpendicular to the horizontal build plate (i.e. the Z_M in figure 13). Thus, it is justified to expect the prior β columnar grain longitudinally directed in the 0° specimens, and transversely directed in the 90° specimens. As a matter of fact, it is possible to say that these angles correspond to the angle between the construction direction and the solicitation direction, i.e. the angle between Z_M and Y_S.
The stress state was:

$$\boldsymbol{\sigma} = \begin{bmatrix} 0 & 0 & 0 \\ 0 & \sigma_{yy} & 0 \\ 0 & 0 & 0 \end{bmatrix} \qquad \boldsymbol{\varepsilon} = \begin{bmatrix} -\nu\varepsilon_{yy} & 0 & 0 \\ 0 & \varepsilon_{yy} & 0 \\ 0 & 0 & -\nu\varepsilon_{yy} \end{bmatrix} \tag{1}$$

The tests were conducted according to a displacement control: the testing system was set to provide a displacement of 0.9 mm/min.

This value was chosen in order to obtain a strain rate of 0.001 Hz; since the length of the measured part of the specimen was 15 mm:

$$\dot{\varepsilon} = \frac{v}{l} \Rightarrow v = l \cdot \dot{\varepsilon} = 15mm \cdot 0.001Hz = 0.015mm/s = 0.9mm/min \qquad (2)$$

The measurement system was based on the digital image correlation, since the strain gauge did not perfectly bind to the surface, slipping during the test.
The procedure used for the VIC-3D® software consisted in:

- set the cameras;
- calibrate the system;
- take the images;
- extract the desired data.

Setting the cameras was important to have images into focus from both the cameras, and thus properly capture the displacements of the small black dots spray-painted on the specimens. The calibration step had the same purpose; it was based on the calibration images, photos of a grid taken at different angles.
The images capture was triggered by the starting movement of the testing machine, and ended with the rupture of the specimen, detected by the machine thanks to a sudden drop in the force, measured by the testing system. The frequency of image acquisition was set to 100 ms.
Once the test was completed, it was time to move to the analysis phase. For this phase, it was necessary to select a reference image (in this case the first image was always chosen as reference), define a rectangular region of analysis and a step size, i.e. the size of the squares composing the analysis region (in this case the size was chosen in order to have 5-7 black dots in a square). This procedure is shown in figure 17.

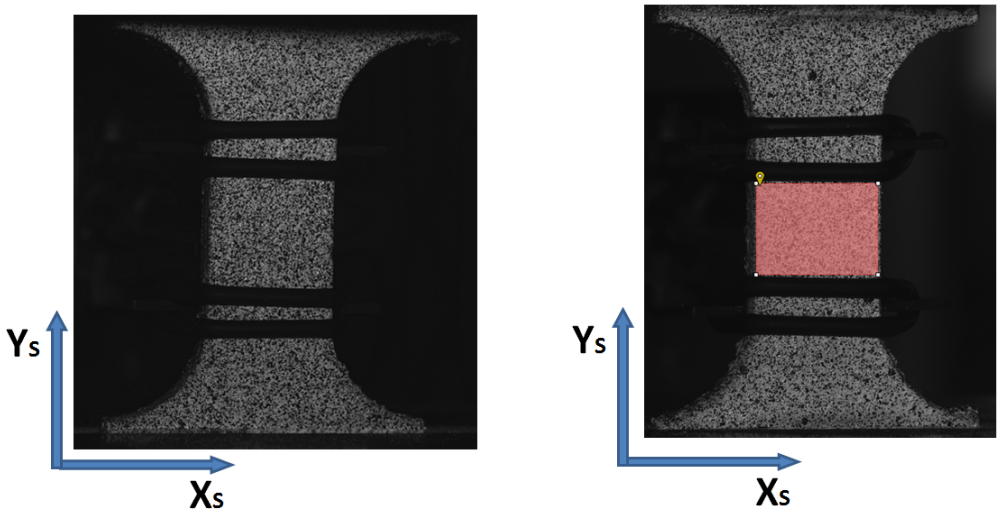

(a) Image acquired during a test. The black stripes are rubber bands to fix the strain gauge

(b) Selection of the area of interest

Figure 17: *VIC-3D® processing*

The software could then extract the average data in the selected area for each image (in CSV format), in particular: coordinates and displacements in three directions (vertical, horizontal, out-of-plane), as well as the components of the Lagrange strain tensor and the principal strains. Moreover, it was possible to add a virtual strain gauge in the vertical direction, used to confirm the strain results (displayed in figure 18). Nevertheless, it was observed for every specimen that the data coming from the average Lagrange strains was coincident to that coming from the virtual strain gauges, as shown in figure 19; therefore the shown result came from the average strains.
The data, in particular in this case the vertical strain, was then associated to the engineering stress (obtained dividing the force provided by the testing system by the original area) to obtain the stress-deformation diagrams for every specimen.
A summary for the procedure is represented in figure 20.
From the stress-deformation diagrams, like the one shown in figure 21 it was possible to obtain:

- the UTS (Ultimate Tensile Strength): the maximum tolerated stress before breaking;
- the rupture strain: the maximum tolerated strain before breaking, measure of the ductility of the specimen;
- the Young modulus: the slope of the stress-strain curve in the linear elastic regime, measure of the stiffness of the specimen;

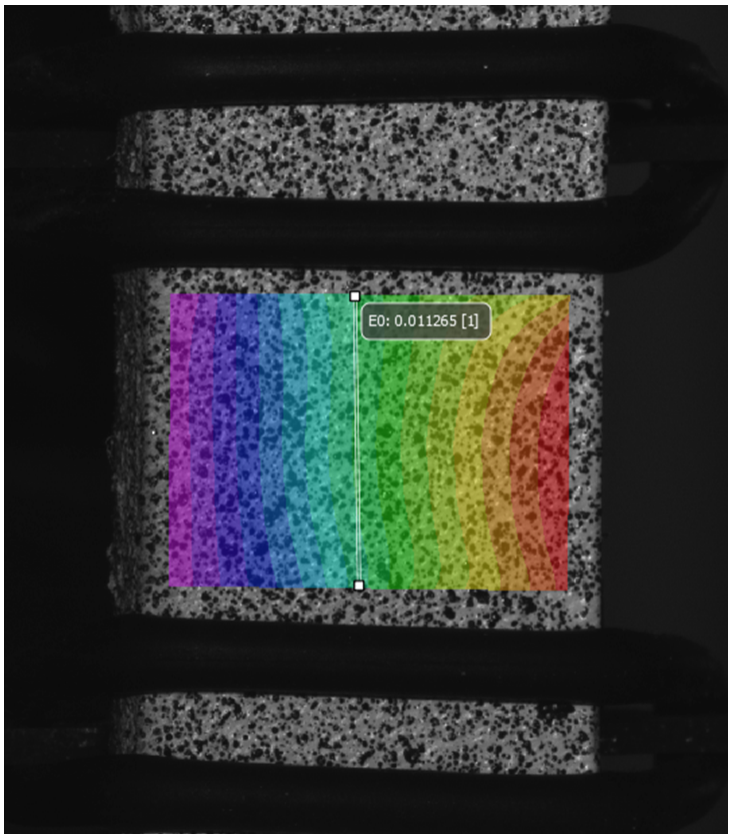

Figure 18: *Data visualization for vertical strain*

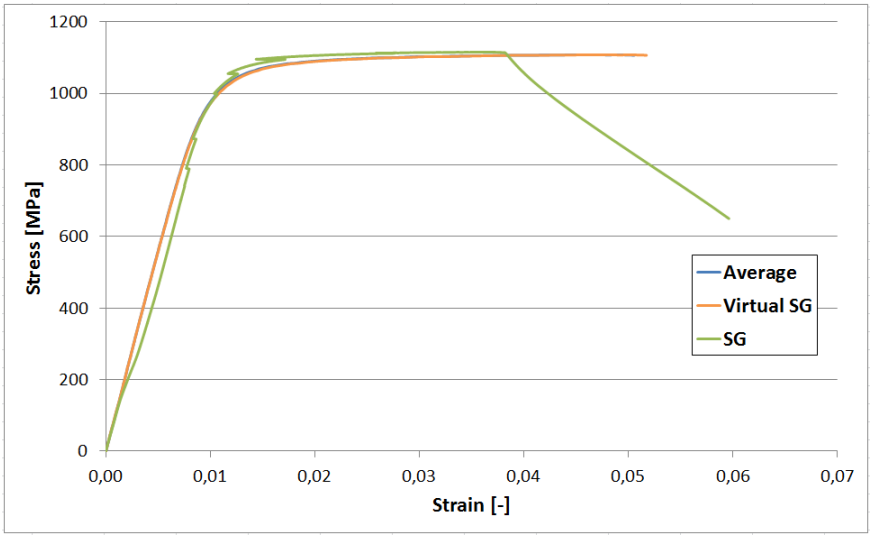

Figure 19: *Stress-strain curves obtained through different methods. The "Average" and the "Virtual SG" are coincident. The slipping of the strain gauge is evident in "SG"*

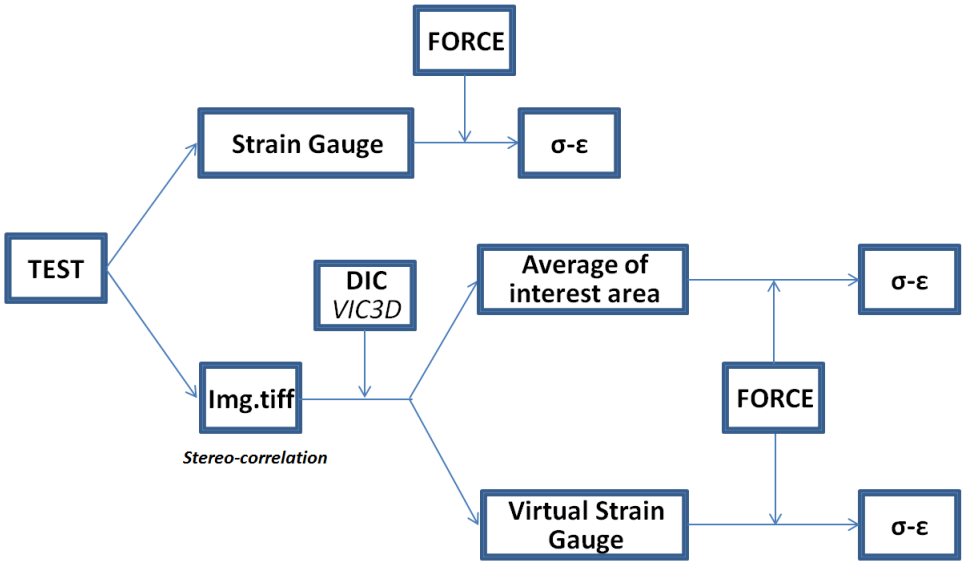

Figure 20: *Post-treatment process for tensile tests*

- the yield stress: the stress at which the specimen began to deform plastically. In this case, the value was obtained by defining a straight line with the same slope of the curve in the linear elastic regime (thus the Young modulus), with an offset for the strain of 0.2%: the intersection between the stress-strain curve and this line was the yield point.

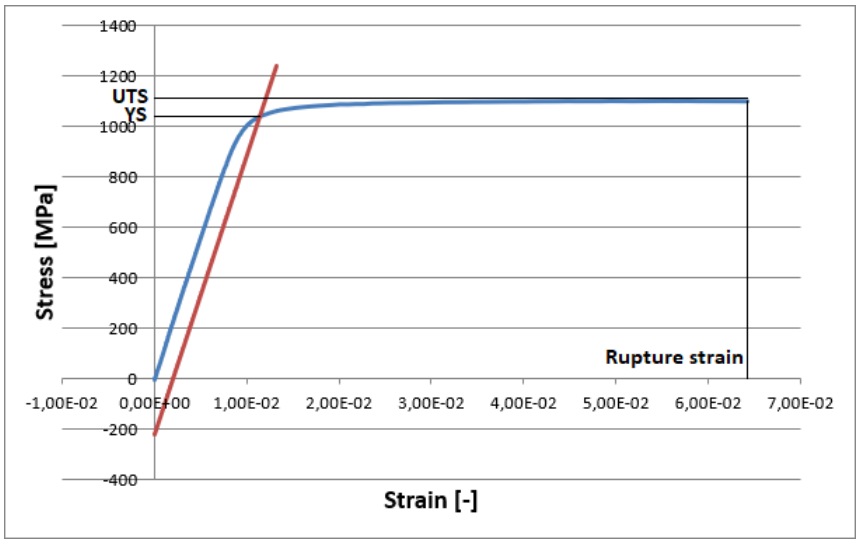

Figure 21: *Stress-strain diagram obtained for one of the specimens. The straight line has been drawn to identify the yield stress*

2.2.4 Shear tests

The available specimens for the shear tests were 16, as specified in table 6. Their geometry is displayed in figure 22.

Identification Number	Orientation (°)
63-64-65-66-67-68	0
41-42	30
43-44-45	45
46-47	60
48-49-50	90

Table 6: *Available shear specimens*

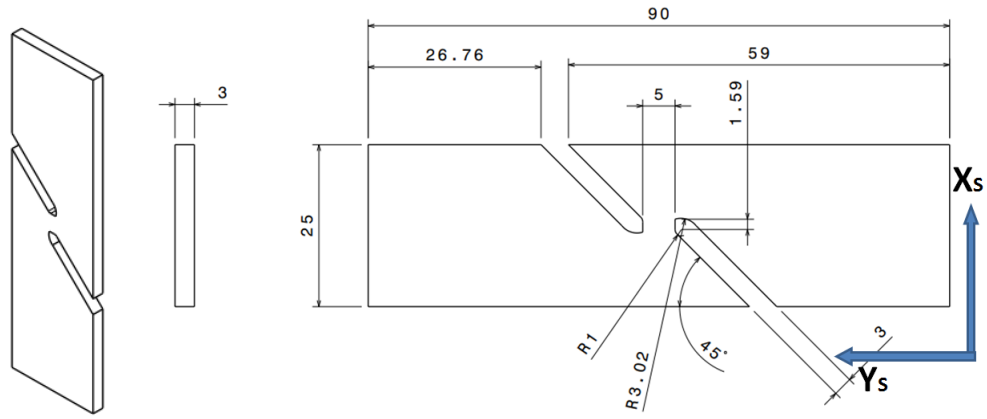

(a) Isometric view

(b) Specimen geometry

Figure 22: *Specimen for shear test*

As already explained these angles are taken with respect to the vertical direction, perpendicular to the horizontal build plate.
As for the uniaxial tensile tests, a displacement control was applied, with the testing system set to provide a displacement of 0.9 mm/min.
The specimens were designed in order to have an initially rectangular shearing zone of dimensions 5 *mm* and 1.59 *mm*. This zone was deformed during the test, to become a non-rectangular parallelogram, with the initially right angles changed (in particular, two decreased and two increased) of a quantity θ during the test, as displayed in figure 23.

The stress state could be in this case approximated to a pure shear stress state:

$$\boldsymbol{\sigma} = \begin{bmatrix} 0 & \sigma_{xy} & 0 \\ \sigma_{xy} & 0 & 0 \\ 0 & 0 & 0 \end{bmatrix} \qquad \boldsymbol{\varepsilon} = \begin{bmatrix} 0 & \varepsilon_{xy} & 0 \\ \varepsilon_{xy} & 0 & 0 \\ 0 & 0 & 0 \end{bmatrix} \tag{3}$$

Where the strain was:

$$\varepsilon_{xy} = \frac{1}{2}\gamma_{xy}, \qquad \gamma_{xy} = tan(\theta) \tag{4}$$

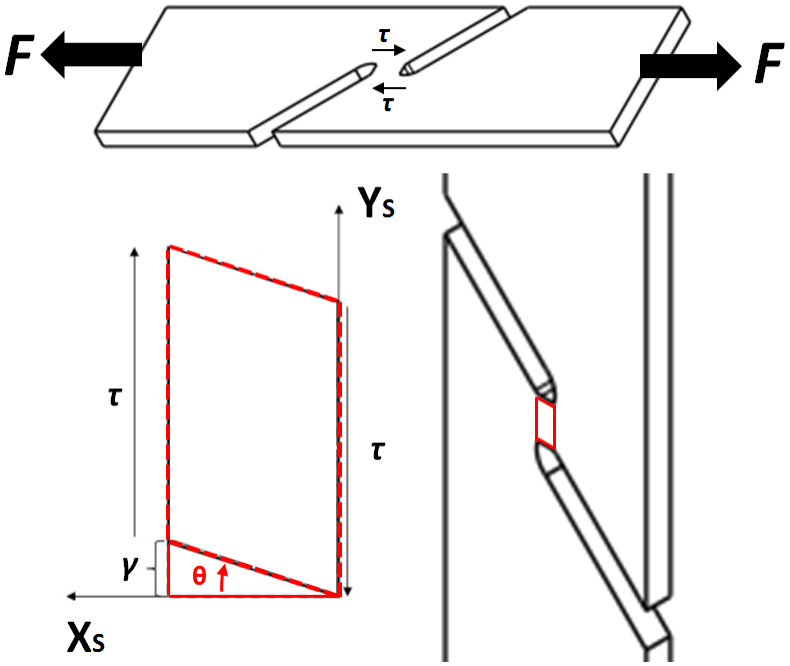

Figure 23: *Shear strain*

The procedure for the image correlation was already described for the uniaxial tensile tests.
An important difference with respect to the previous tests was relative to the strain measure. In fact, the considered component of the strain tensor was ε_{xy}, and in this case the vertical virtual strain gauge was not used, since it could not confirm the validity of the considered data.
Instead, during the analysis phase on the image correlation software, it was hypothesized to use another technique to confirm the results: three points in the area of interest were analyzed; these points at the beginning of the test (non-deformed specimen) were at the vertices of an imaginary right-angled triangle.

During the test, the points moved, and the initially right angle was changed of a quantity θ. Calculating the tangent of θ, it was possible to obtain another measure of the strain, in addition to the average value in the area of interest automatically provided by the software.
The calculation process is schematized in figure 24.

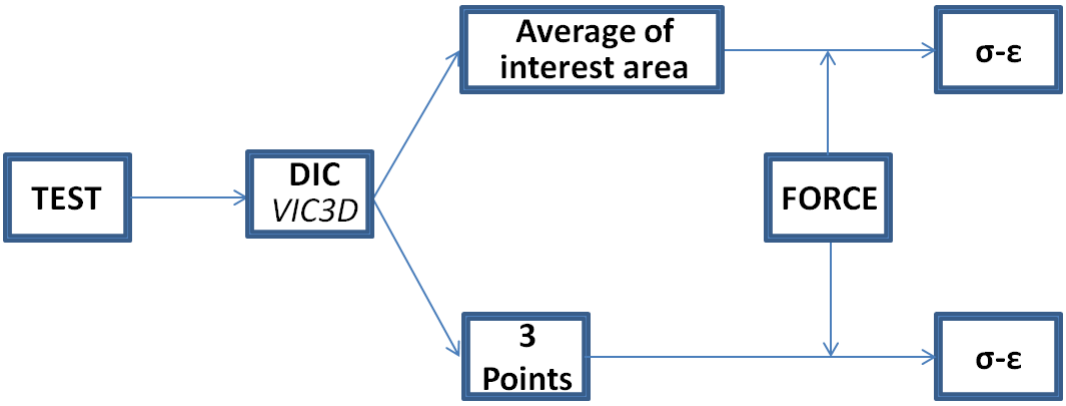

Figure 24: *Post-treatment process for the shear tests*

Unlike the uniaxial tensile tests, in this case the results coming from the two methods were slightly different. It was chosen to develop the analysis from the average Lagrange strains, which for every specimen provided a shear modulus closer to the expected value (i.e. the reference value for annealed specimens) with respect to the other system.
The shear stress could be determined from [44]:

$$\sigma_{xy} = \tau = \frac{F}{h_0 \cdot w_0} \tag{5}$$

Where the force was provided by the testing system. Having the stress and the strain, it was finally possible to draw the stress-strain curves for every test. From these diagrams, it was possible to obtain:

- the USS (Ultimate Shear Strength): the maximum tolerated shear stress before breaking;
- the rupture strain: the maximum tolerated shear strain (ε_{xy}) before breaking, measure of the shear ductility of the specimen;
- the shear modulus: the slope of the shear stress-strain curve in the linear elastic regime, measure of the shear stiffness of the specimen;
- the shear yield stress: the shear stress at which the specimen began to deform plastically. As for the uniaxial tensile tests, this value was obtained by the use of a straight line with an offset of 0.2% for the strain, intersecting the stress-strain curve.

Moreover, to have a numerical comparison for the results, the shear specimen was modelled using the simulation software Abaqus FEA, as shown in figure 25.

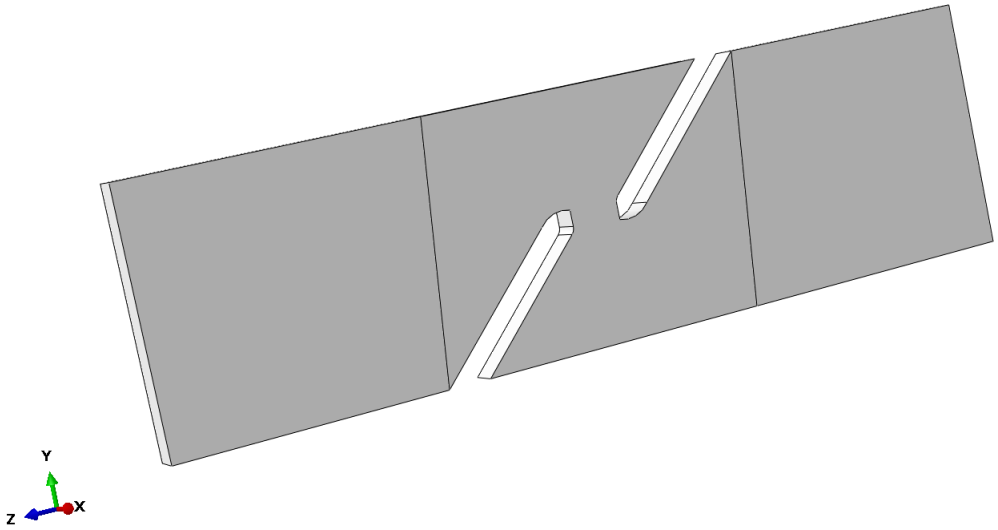

Figure 25: *Shear specimen modelled on Abaqus FEA*

The material characterization was based on average values from every conducted test. The boundary conditions, displayed in figure 26 consisted of a fixed face on one side of the specimen, and a displacement was applied on the face at the other side.

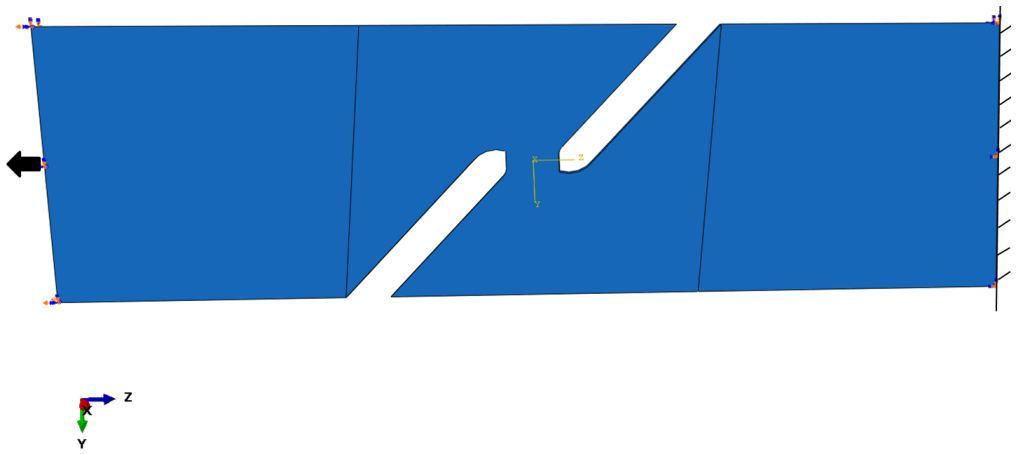

Figure 26: *Boundary conditions applied for the numerical model*

The mesh was designed in order to have quite fast calculations, but still precise results in the shear zone. Thus, the mesh was refined in correspondence of that area of the specimen, as shown in figure 27.

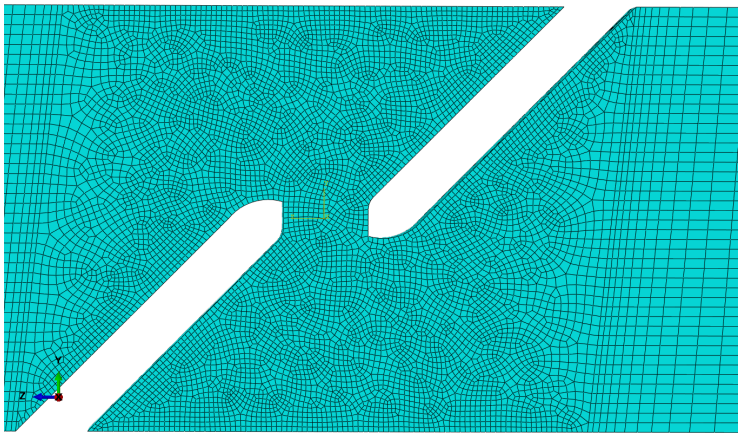

Figure 27: *Detail of the mesh in the shear zone*

The results of the simulation confirmed that the stress and the strain were confined to the shearing zone. Moreover, as can be seen in figure 28, the deformation isovalues were disposed in diagonal direction both in the numerical and the experimental tests.

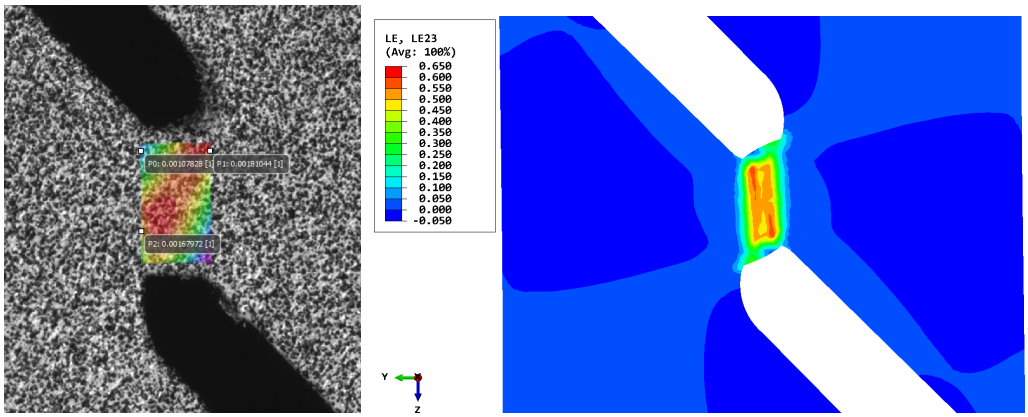

(a) From VIC-3D®

(b) From Abaqus FEA

Figure 28: *Visualization for the shear strain*

2.3 Results and discussion

2.3.1 Uniaxial tensile tests

Due to some problems with the measurement system, only 11 specimens provided all the useful data, shown in table 7.

Orientation (°)	UTS (MPa)	yield stress (MPa)	E (GPa)	Rupture strain (%)
0	1137.25	1077	114.19	5.49
0	1117.51	982	112.87	11.40
30	1127.09	961	115.90	2.97
30	1097.17	1032	110.16	4.73
45	1109.63	1029	113.92	7.58
45	1100.02	1038	110.53	6.43
45	1118.90	1005	114.83	5.53
60	1117.68	1016	111.43	8.17
90	1107.83	1009	111.83	5.06
90	1108.74	997	112.97	3.79
90	1102.25	1008	109.84	6.75

Table 7: *Results from tensile tests*

Taking the average value with standard deviation for each orientation, and comparing to the reference values for annealed specimens [16], it is possible to obtain the data shown in table 8 and figures 29, 30. A comparison of stress-strain curves for specimen of different orientations is displayed in figure 31.

Orientation (°)	UTS (MPa)	yield stress (MPa)	E (GPa)	Rupture strain (%)
-	950	880	113.8	14
0	1127.38±13.96	1029.5±67.17	113.53±0.93	8.44±4.17
30	1112.13±21.15	996.5±50.20	113.03±4.06	3.85±1.24
45	1109.52±9.44	1024±17.06	113.10±2.27	6.51±1.03
60	1117.68	1016	111.43	8.17
90	1106.27±3.51	1004.67±6.66	111.55±1.58	5.20±1.48

Table 8: *Results from tensile tests - Average values for each orientation*

Looking at this table it is possible to observe that:

- All the strength values (both UTS and yield stress) are higher than the reference value, while all the values of rupture strain are lower. This observation is consistent with the articles found in the bibliography review;
- The maximum strength values (UTS and yield stress) are obtained for 0° specimens, while the minimum ones correspond to the 90° specimens. Also

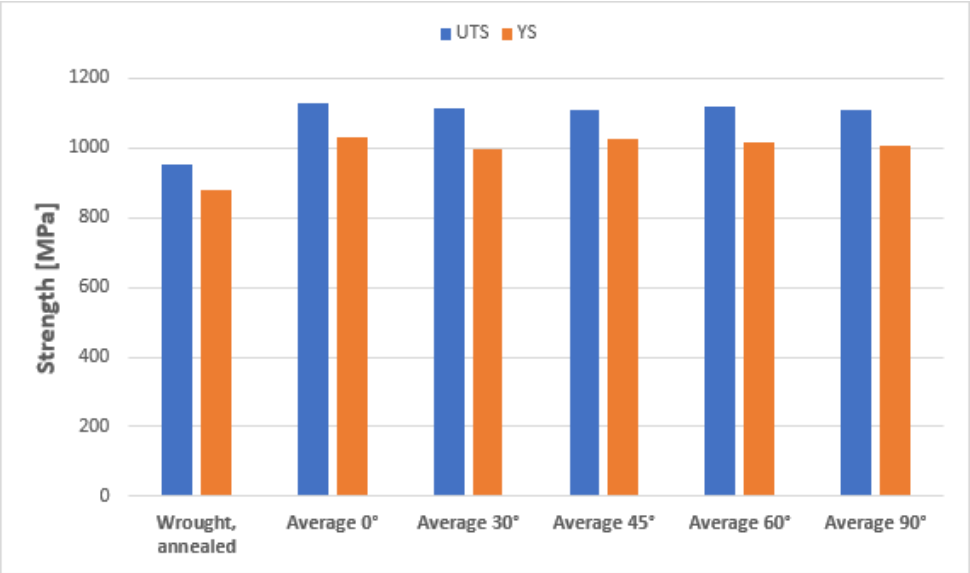

Figure 29: *Results from tensile tests - Average strength values for each orientation*

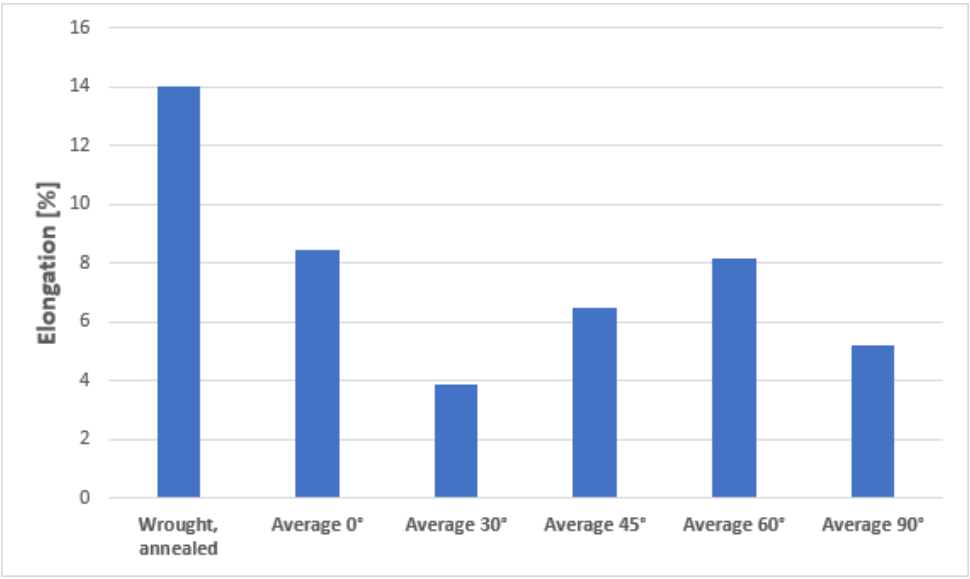

Figure 30: *Results from tensile tests - Average elongation values for each orientation*

this observation is consistent with the consulted papers;

- The maximum rupture strain values are observed in 0° specimens, while the minimum ones are for the 30° specimens. This was not reported in the consulted papers, where the 30° orientation was never analyzed. Nevertheless, the papers showed that, for non heat-treated pieces, the maximum elongation values were obtained for the 0° orientation. In this case, the pieces were subjected to a stress relieving heat treatment; thus, the defects were

not eliminated, and allegedly influenced the weak ductility for 90° specimens, compared to 0° ones;

- The Young modulus values are comparable to the reference value. The maximum values were obtained for 0° specimens, while the minimum ones were found for 90° specimens; nevertheless, the differences are quite limited, as observed in the consulted articles.

Moreover, the value of Poisson ratio was determined for every specimen, dividing the horizontal strain by the vertical one. The results showed no anisotropy, and were coincident with the reference value ($\nu = 0.33$).

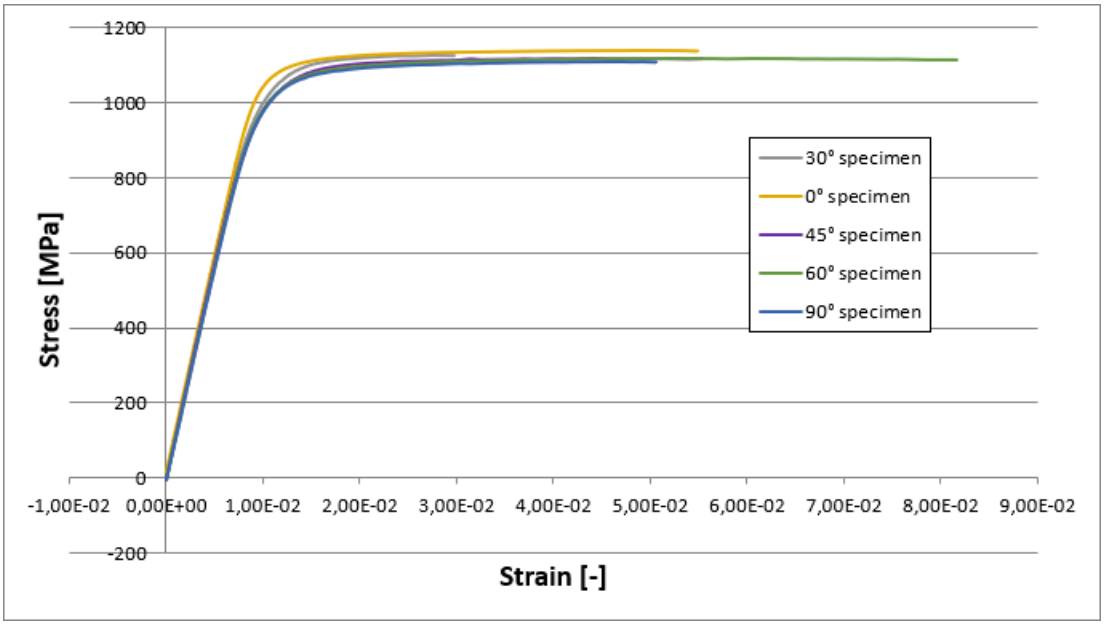

Figure 31: *Results from tensile tests - Stress-strain curves for a specimen for each orientation*

2.3.2 Shear tests

Due to some problems with the measurement system, only 14 specimens provided all the useful data, shown in table 9.

Orientation (°)	USS (MPa)	yield stress (MPa)	G (GPa)	Rupture strain (%)
0	417.13	-	39.78	0.59
0	436.2	-	43.46	0.58
0	459.87	458	39.63	0.69
0	461.63	-	37.26	0.68
0	463.81	-	38.40	0.64
30	586.34	528	40.96	1.32
30	581.52	489	43.21	1.15
45	615.93	503	40.43	1.55
45	618.78	478	39.44	1.88
60	551.05	472	43.05	0.96
60	608.48	513	38.44	1.50
90	432.47	-	37.91	0.62
90	441.46	-	40.47	0.61
90	513.57	486	41.49	0.80

Table 9: *Results from shear tests*

Taking the average value with standard deviation for each orientation, and comparing to the reference values for annealed specimens [16], it is possible to obtain the data shown in table 10. From the test results it is possible to observe the

Orientation (°)	USS (MPa)	yield stress (MPa)	G (GPa)	Rupture strain (%)
-	550	-	44	-
0	447.73±20.42	458	39.70±2.34	0.64±0.05
30	583.93±3.41	508.5±27.58	42.08±1.59	1.24±0.12
45	617.36±2.01	490.5±17.68	39.93±0.70	1.72±0.23
60	579.77±40.61	492.5±28.99	40.75±3.26	1.23±0.38
90	462.50±44.46	486	39.96±1.84	0.68±0.11

Table 10: *Results from shear tests - Average values for each orientation*

following:

- In this case not all the strength values are greater then the reference value, in contrast to what was observed for the uniaxial tensile tests;
- Considering the USS, the lowest values correspond to the 0° specimens, with the 90° specimens second lowest, and both the 0° and the 90° components show lower values than the reference for wrought and annealed.

The best results in terms of USS are obtained for the 45° specimens. Indeed, with this orientation, the prior β grains are aligned with the direction of principal solicitation; thus, this result corresponds to the highest UTS for 0° specimens in the tensile tests;

- Not every specimen reached the yielding point, showing a ductile behavior: almost every 0° and 90° specimen experienced a fragile fracture.
  Instead, for the other orientations, the yield point was always reached, and the highest values were reached with the 30° specimens. As there is no reference value for shear yield stress in the literature, it was not possible to compare with the values for wrought parts;
- The shear modulus values are smaller than the reference value; the highest results are obtained for 30° specimens. Nevertheless, there is not a significant difference among the values correspondent to the various orientations;
- The rupture strain values show a clear distinction between the 0° and 90° specimens, that had almost in every case a fragile behavior, and the others, that instead reached the yielding point. The most ductile behavior was observed for the 45° specimens, possibly because of the coincidence between the principal direction of solicitation and the prior β grains orientation. As for the USS, this result can be connected to the behavior showed by the 0° specimens in the tensile tests.

As already explained, the numerical simulation confirmed the mechanical behavior observed in the experimental tests. Moreover, tracing the stress-strain diagram for the average of the value in the elements from the shearing zone, it was possible to observe that the stress values are coherent with the obtained data: in fact, the UTS was 555 MPa, and the yield stress was about 410 MPa (in this case it was not possible to find the exact value, since the diagram was traced on Abaqus), both not far from the average of the experimental results. A comparison of the different stress-strain curves obtained is shown in figure 32.

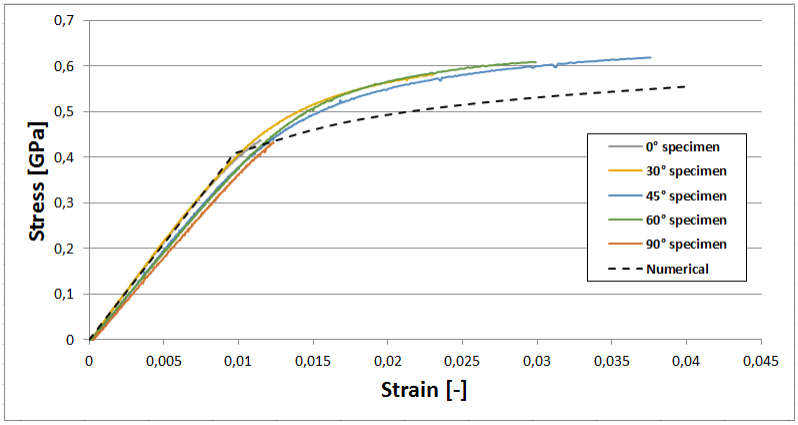

Figure 32: *Results from shear tests - Stress-strain curves for a specimen for each orientation*

From the experimental data, it was possible to calculate the equivalent Von Mises stress [45]:

$$\sigma_{eq} = \sqrt{3} \cdot \sigma_{xy} \tag{6}$$

And the equivalent Von Mises strain [46]:

$$\varepsilon_{eq} = \frac{2 \cdot \varepsilon_{xy}}{\sqrt{3}} = \frac{\gamma_{xy}}{\sqrt{3}} \tag{7}$$

Obtaining the values shown in tables 11 (for each specimen) and 12 (average for each orientation, compared to the traction values), and figures 33, 34.

Orientation (°)	USS (MPa)	yield stress (MPa)	Rupture strain (%)
0	722.48	-	0.68
0	755.52	-	0.66
0	796.52	739.28	0.80
0	799.56	-	0.78
0	803.35	-	0.74
30	1015.57	914.52	1.53
30	1007.22	846.97	1.33
45	1066.83	871.22	1.79
45	1071.76	827.92	2.17
60	954.45	817.53	1.10
60	1053.92	888.54	1.73
90	749.07	-	0.71
90	764.63	-	0.70
90	889.54	841.78	0.93

Table 11: *Results from shear tests - Equivalent stress, strain*

Orientation (°)	UTS (MPa)	Yield stress (MPa)	Rupture strain (%)
-	950	880	14
0 - Shear	775.49±35.38	793.28	0.73±0.06
30 - Shear	1011.40±5.90	880.75±47.76	1.43±0.14
45 - Shear	1069.29±3.49	849.57±30.62	1.98±0.27
60 - Shear	1004.19±70.33	853.04±50.21	1.42±0.44
90 - Shear	801.08±77.00	841.78	0.78±0.13
0 - Tensile	1127.38±13.96	1029.5±67.17	8.44±4.17
30 - Tensile	1112.13±21.15	996.5±50.20	3.85±1.24
45 - Tensile	1109.52±9.44	1024±17.06	6.51±1.03
60 - Tensile	1117.68	1016	8.17
90 - Tensile	1106.27±3.51	1004.67±6.66	5.20±1.48

Table 12: *Results from shear and tensile tests - Average equivalent values for each orientation*

Through these values, it was possible to make a comparison with the data obtained for the traction, and the reference values. In particular, it was observed that:

- There was a general worsening of the strength and, especially, of the ductility;
- The 0° specimens, which showed the highest values in strength and rupture strain for the tensile tests, passed instead to the lowest values for the shear tests;
- While for the tensile tests the reference value for UTS was always overcome, for the shear tests only the 30°, 45° and 60° specimens reached greater values than the reference;
- While for the tensile tests the reference value for yield stress was always overcome, for the shear tests the yielding was not always reached; moreover, even when the yielding was reached, the average value of yield stress was lower than the reference value, except for the 30° specimens, who reached approximately the same value registered for wrought, annealed specimens;
- The rupture strain values for the shear specimens are extremely low compared to the ones obtained from the tensile tests, and even lower compared to the reference value.

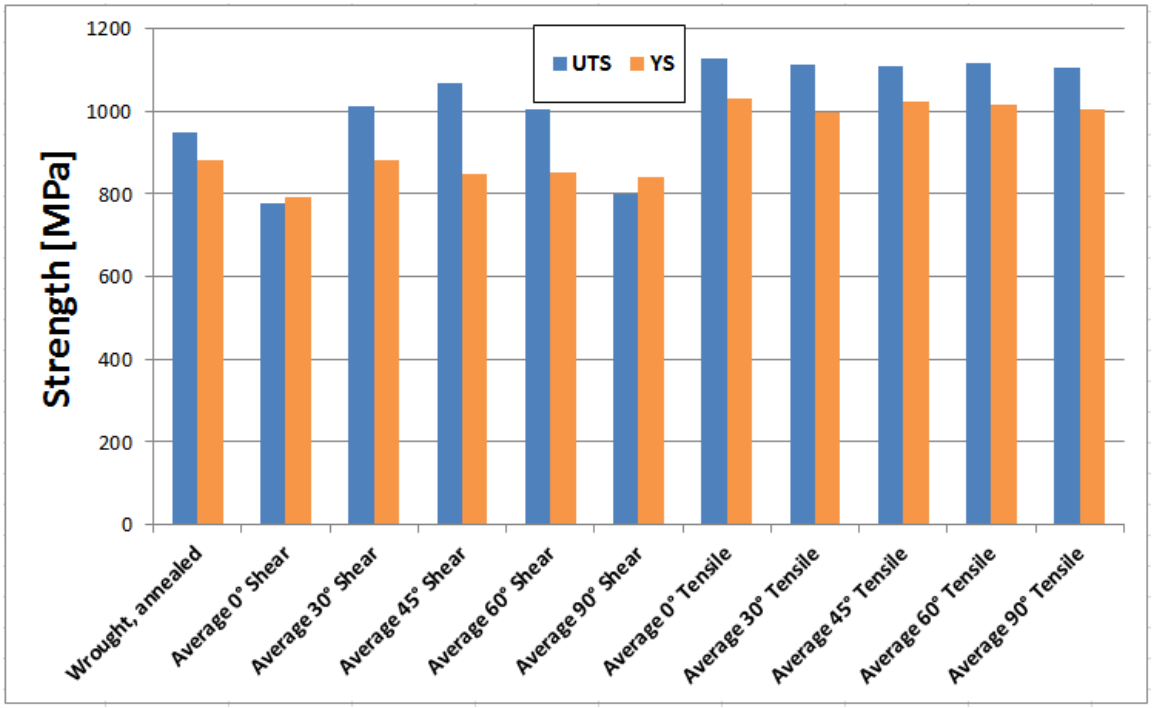

Figure 33: *Results from shear and tensile tests - Average equivalent strength values for each orientation*

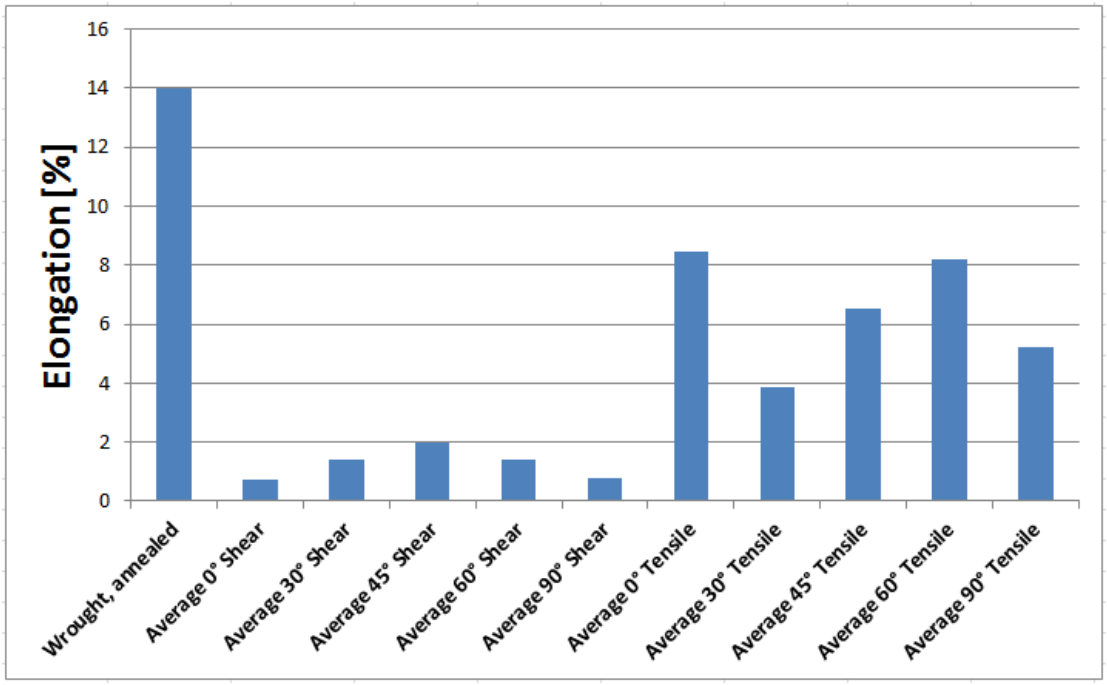

Figure 34: *Results from shear and tensile tests - Average equivalent strain values for each orientation*

2.4 Conclusion

In this part of the project, various tests were conducted in order to analyze the anisotropy of the mechanical behavior of the titanium alloy Ti6Al4V produced by SLM.
This type of unidirectional manufacturing can induce an anisotropic microstructure, consisting of prior β columnar grains and fine acicular α' grains: the direction of the former, coincident with the build direction, can influence the behavior, as well as the presence of defects, such as lack-of-fusion pores.
For the tensile tests, consistently with the consulted articles, especially ones who studied samples without the application of a HIP treatment (capable of eliminating the defects), the best results in term of ductility were obtained for specimens tested along the build directions; these specimens provided also the best results in terms of strength. However, the strength results do not show a significant difference among the different orientations. This might be due to the acicular α' grains, that decrease the differences among directions.
Nevertheless, the results show, comparing to the reference values for wrought, annealed specimens, better results in terms of strength, and worse results in terms of rupture strain.
For the shear tests, the best results in terms of ductility were obtained for specimens whose build direction was parallel to the direction of principal stress, i.e. 45°; the same was observed for the strength. This observation is consistent with the tensile results for the 0° specimens.
In this case, the results were compared to the tensile data through Von Mises theory, and it was observed that the ductility is significantly decreased for every orientation, while the strength is significantly decreased for the 0° and 90° specimens

3 Fatigue behavior of stainless steel 316L manufactured by SLM

3.1 Bibliography report

The 316L stainless steel (SS316L) is a member of the austenitic steels that was developed more than three decades ago for fast-breeder reactor applications within the EU countries. Its chemical composition consists of [48]:

- Carbon (maximum weight: 0.03%)
- Manganese (maximum weight: 2.0%)
- Silicon (maximum weight: 0.75%)
- Phosphorus (maximum weight: 0.045%)
- Sulfur (maximum weight: 0.03%)
- Chromium (maximum weight: 18.0%; minimum weight: 16.0%)
- Molybdenum (maximum weight: 3.0%; minimum weight: 2.0%)
- Nickel (maximum weight: 14.0%; minimum weight: 10.0%)
- Nitrogen (maximum weight: 0.1%)

The SS316L has both good weldability and machinability and in combination with high corrosion resistance it can be used in a wide range of applications [47], including for exhaust components, high temperature engine and structural parts in aircrafts.
As already highlighted in this report, more than half of all the publications on SLM from 1999 to 2014 concerned steel and titanium, especially 316L stainless steel and Ti6Al4V alloy.
For this part of the project, an analysis on the fatigue behavior of SS316L was performed, conducting tensile, bending and torsional tests on samples manufactured by SLM technique.
Nowadays, a large number of components in the aeronautic domain, as for example the parts of the engines or the blades of the turbines, experience often solicitations provoked by cyclic loads characterized by very high frequencies, than can exceed, during a typical lifespan, a million of cycles [49].
When a great amount of cycles is reached, it is possible to introduce the concept of High Cycle Fatigue (HCF). HCF is a type of fatigue that is connected to small deformations and a great number of cycles to lead to the collapse of the solicited component.

To analyze a cyclic solicitation, it is necessary to consider the mean and alternating stresses. The mean stress is influenced by the the residual stress, produced during the manufacturing.
HCF implies lower stresses with respect to the Low Cycle Fatigue (LCF) and the elastic limits. Moreover, there is not plastic deformation on a macroscopic scale, unlike in the LCF: the main deformation in the HCF is elastic deformation [50].
Fatigue is a localized phenomenon, whose fracture mechanism is, in general, due to the concentration of efforts induced by manufacturing defects [51], in most cases gas pores and lack-of-fusion defects [52].
Fatigue crack propagation usually begins from relatively large pores, located on the surface of a component (or near the surface) or, more rarely, from non-melted particles on the surface. Interior pores represent an additional source of defects when the cracks propagate and merge, forming a critical crack that ends up destroying the part [53, 54, 55]. It is necessary to consider the shape of the defects and their proximity to the surface, as well as their size [52]. The breaking surface is generally flat and perpendicular to the load axes [54]. The specimens whose build direction is normal to the load direction have proven to be less resistant than those with parallel build and load directions [53, 56, 57].
A common solution adopted to reduce the defects consists in an application of Hot Isostatic Pressing (HIP). The HIP treatment implies the simultaneous application of an elevated temperature and an elevated pressure. The isostatic pressure is exerted by a gas (generally inert). Under this conditions, the pores collapse [58], thus the resistance of the material is consistently raised [51, 52, 53, 56]. Moreover, it was remarked that the treatment can increase the ductility of the material [56].
The mechanism of pore collapsing is based on the following formula [58]:

$$p = \frac{2\delta}{r} \tag{8}$$

Where p is the necessary pressure for the collapse, γ the specific energy of the pore internal surface, and r is the pore radius curvature. For a spherical pore r is the radius, but for a more complex shape the surface can be divided into various parts having different curvatures. When the surface is cave inside the pore, r is positive, while when it's convex, r is negative.
From this equation, it is possible to observe that the small pores require a greater collapse pressure than the big ones.
Nevertheless, the HIP treatment is not able to suppress the defects on the surface [52]. Roughness of the AM products is greater than the usual values for conventional products. The arithmetic average roughness Ra obtained through SLM is between 5 and 30 μm [59]. These values depend on the production parameters and on the surface orientation [60]. A control on roughness is important, since it can induce a load concentration on the surface of the part, thus a premature failure.

Usually, mechanical polishing processes are practiced to eliminate the surface pores, and assure a good surface state. This treatment can significantly improve the fatigue resistance of the materials [52]. Moreover, it was remarked that the surface finishing is more influencing on the fatigue resistance than a HIP treatment. Generally, both the treatments are applied, to obtain a high value of endurance limit.
Another important aspect to consider for AM is the residual stress. In fact, their presence can lead to localized deformations that severely influence the fatigue resistance [61, 62, 63].
For the medium and long-term applications, the compression residual stress can improve the fatigue behavior of a part, retarding the cracks initiation and slowing down their propagation. On the contrary, the tension residual stress can facilitate the opening of the cracks from the surface [64].
Residual stress can be reduced by heating the fabrication plate, by mechanical post-treatment, by sandblasting, or by heat treatment [51, 32].
A review of existing articles has shown that, in general, a surface treatment and a HIP improve the endurance limit. Nevertheless, it was also remarked that the surface treatment has the greatest influence on the limit, while the heat treatment slightly improves the values or, in one case, the HIP degraded the fatigue resistance [65], as can be seen in table 13 and figure 35. The three different surface conditions reported in literature are represented in figure 36.

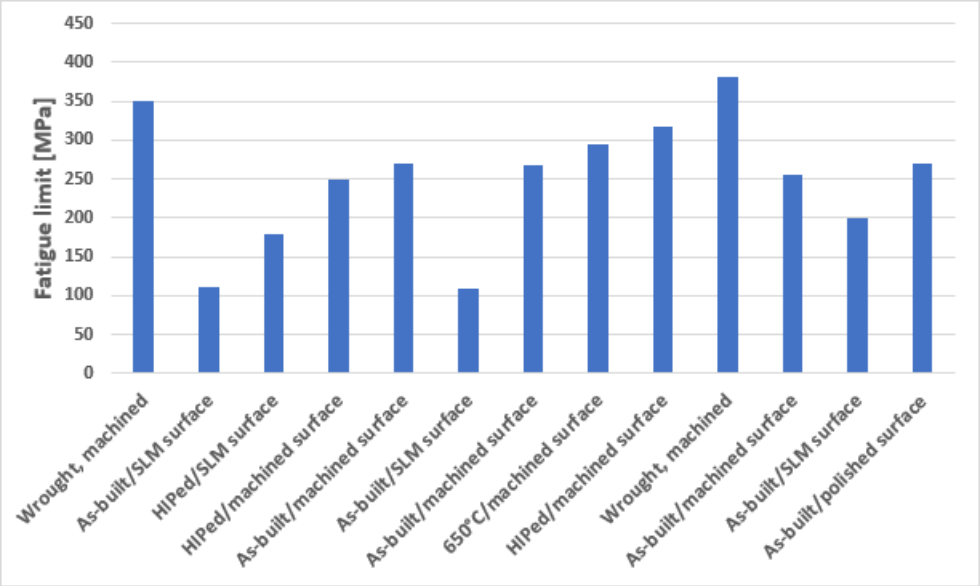

Figure 35: *Summary of fatigue limits for 316L stainless steel for different heat and surface treatments reported in literature [53, 66, 67, 68]*

Reference	Condition (heat/surface)	Fatigue limit (MPa)
[53]	Wrought, machined	350
[53]	As-built/SLM surface	110
[53]	HIPed/SLM surface	180
[53]	HIPed/machined surface	250
[53]	As-built/machined surface	270
[66]	As-built/SLM surface	108
[66]	As-built/machined surface	267
[66]	650℃/machined surface	294
[66]	HIPed/machined surface	317
[67]	Wrought, machined	381
[68]	As-built/machined surface	255
[68]	As-built/SLM surface	200
[68]	As-built/polished surface	269

Table 13: *Summary of fatigue limits for 316L stainless steel for different heat and surface treatments reported in literature*

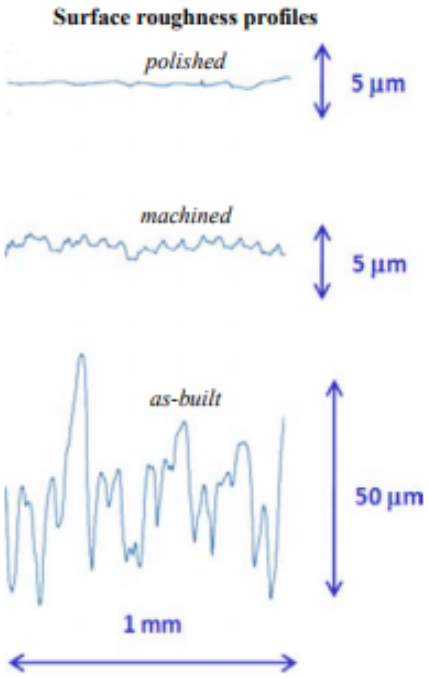

Figure 36: *Representation of the three different surface finishes [68]*

3.2 Experimental study

3.2.1 Introduction

The purpose of this study is to analyze the fatigue behaviour of various specimens of 316L stainless steel, tested after different surface treatments (as-built, polished, machined and polished), in bending, torsion and traction.

3.2.2 Description of the samples

For this part of the project three types of samples have been used: flat samples for the bending tests, cylindrical samples with square extremities for the torsional tests and cylindrical samples with circular extremities for the tensile tests.
Two identical trays, each with 80 specimens, as displayed in figure 37, were manufactured using the production parameters shown in table 14.

Labeling rate	1400 mm/s
Slew rate	5000 mm/s
Laser power	129 W
Spacing	50 μm
Strategy	Hexagonal (island pattern)
Overlap between hexagons	100 μm
Laser spot size	70 μm

Table 14: *Production parameters for the manufacturing of the SS316L specimens*

As for the Ti-6Al-4V, the samples have been subjected to a stress relieving heat treatment in a protective atmosphere, consisting of heating at 620℃, holding the temperature for 90 minutes, and finally slowly cooling to room temperature, as shown in figure 38.
The arithmetic average roughness Ra was measured for the as-built specimens, giving a value between 120 and 200 μm.
The surfaces of some specimens of each kind were polished using Silicon Carbide abrasive paper of different grits, beginning from 60, until 1200/4000. The polishing was finished with a diamond polishing paste of 10 μm; this final passage was performed on a rotating machine, a a rotating velocity of 2000 rpm.
For the bending and torsional tests, other specimens were machined, eliminating 0.25 mm from the surface, and then polished with abrasive paper and diamond paste.

(a) As-built tray

	Nombre	Géométrie
	30	G1-epv F torsion
	30	G2-epv F flexion
	5	G3-epv traction
	5	Cylindre Φ8 X 10
	5	Cylindre Φ4 X 10
	5	Cylindre Φ2 X 10

(b) Detail on the specimens produced. Only the G1, G2, G3 have been used in this project

Figure 37: *Manufacturing of the SS316L specimens*

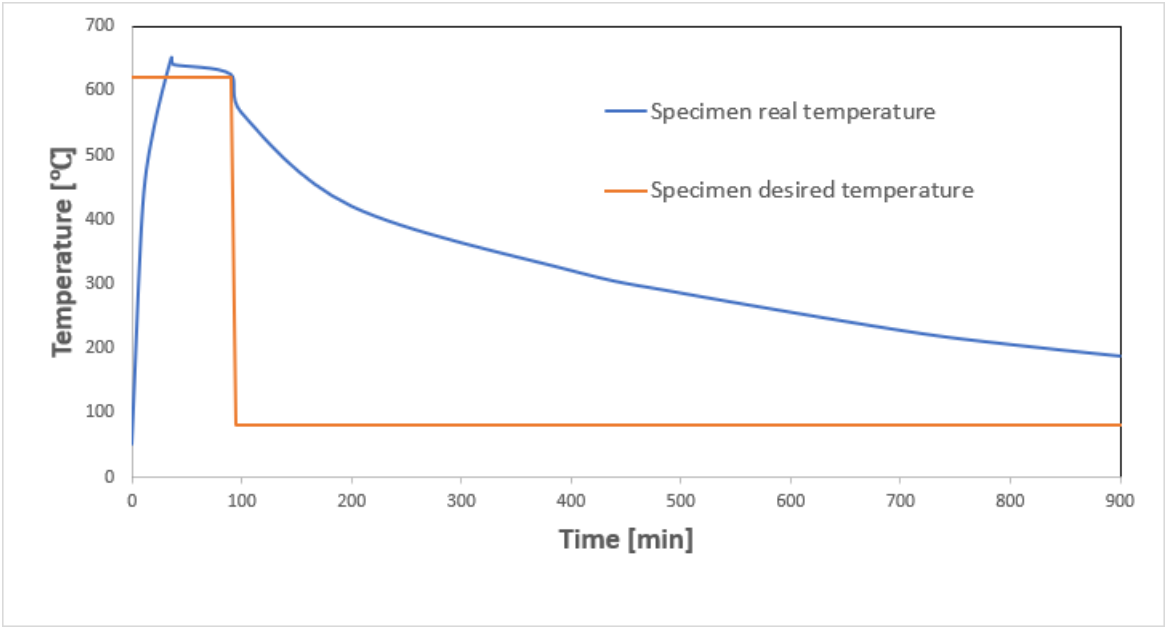

Figure 38: *Stress relieving heat treatment*

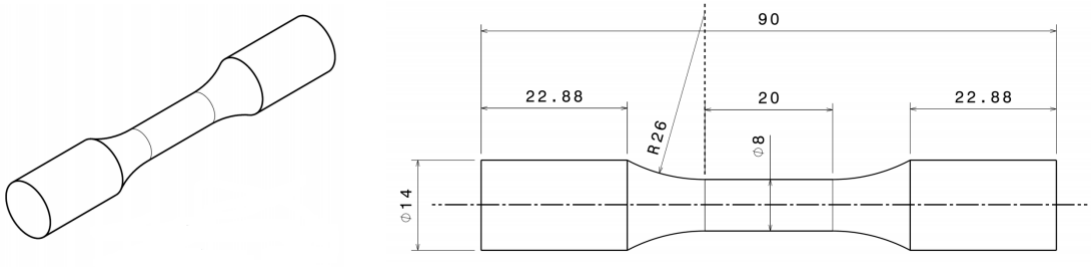

Figure 39: *Tensile specimen geometry*

3.2.3 Tensile fatigue tests

The geometry of the tensile specimens is detailed in figure 39. The tests were conducted on a biaxial servohydraulic testing system for tensile and torsional tests: Instron® 8874, displayed in figure 40, at a frequency of 15 Hz. The machine was set to provide an oscillating value of force between two extremities of opposite sign, but equal absolute value: R=-1.

Figure 40: *Biaxial testing system used for the tensile tests*

These extremities were chosen in order to provide a determined value of stress, knowing the diameter of the circular specimens:

$$F = \frac{\sigma}{\frac{\pi \cdot d^2}{4}} \tag{9}$$

The stress value, in turn, was chosen by using the staircase method [69], exemplified in figure 41. In this method the first specimen is subjected to a stress corresponding to the expected average fatigue strength. If the specimen survives $2 \cdot 10^6$ cycles, it is discarded and the next specimen is subjected to a stress that is one increment above the previous, i.e. a survivor is always followed by the next using a stress one increment above the previous. The increment corresponds to the expected value of standard deviation. When a specimen fails prior to reaching $2 \cdot 10^6$ cycles, the obtained number of cycles is noted and the next specimen is subjected to a stress that is one increment below the previous.
Once the test is completed, it is possible to calculate the value of endurance limit and its standard deviation: to do that, it is necessary to determine the less frequent event between failure and run-out of the specimen; then the limit is:

$$\sigma_D = \sigma_0 + d \cdot (\frac{A}{F} \pm \frac{1}{2}) \tag{10}$$

- $+$ if the less frequent event is run-outs;
- - if the less frequent event is failure.

The standard deviation can be found by:

$$s = 1.62 \cdot d \cdot (\frac{F \cdot B - A^2}{F^2} + 0.029) \tag{11}$$

Where:

- σ_0 is the lowest stress level for the less frequent occurrence;
- d is the stress increment;
- $F = \sum f_i$;
- $A = \sum i \cdot f_i$;
- $A = \sum i^2 \cdot f_i$;
- i is the stress level numbering;
- f_i is the number of samples at stress level i.

The formula for the standard deviation is an approximation and can be used when:

$$\frac{B \cdot F - A^2}{F^2} > 0.3 \tag{12}$$

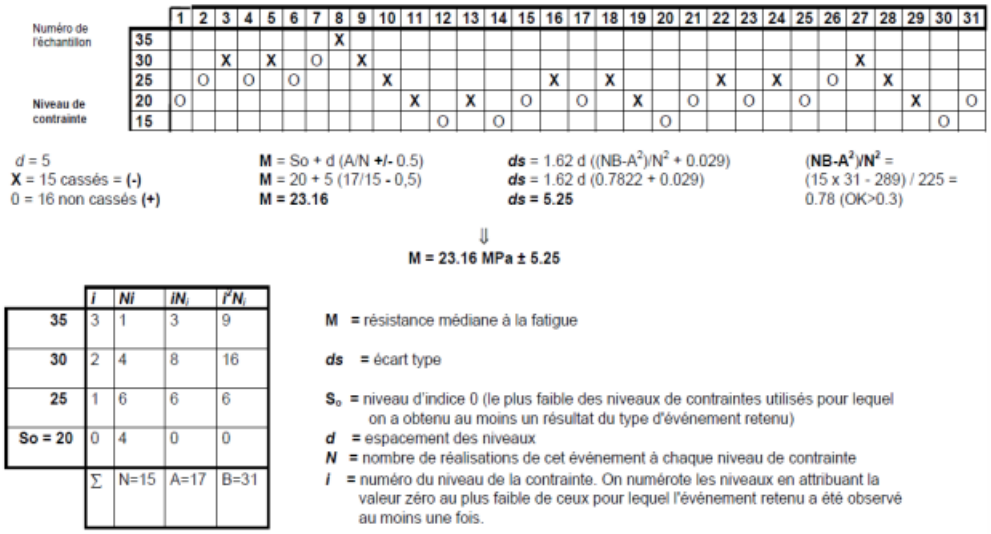

	i	*Ni*	*iNi*	*i²Ni*
35	3	1	3	9
30	2	4	8	16
25	1	6	6	6
So = 20	0	4	0	0
	Σ	N=15	A=17	B=31

M = résistance médiane à la fatigue

ds = écart type

$\mathbf{S_o}$ = niveau d'indice 0 (le plus faible des niveaux de contraintes utilisés pour lequel on a obtenu au moins un résultat du type d'événement retenu)

d = espacement des niveaux

N = nombre de réalisations de cet événement à chaque niveau de contrainte

i = numéro du niveau de la contrainte. On numérote les niveaux en attribuant la valeur zéro au plus faible de ceux pour lequel l'événement retenu a été observé au moins une fois.

Figure 41: *Example of application of staircase method*

Two different staircases methods were applied, one for the as-built specimens and one for the polished specimens. After the completion of the staircases, the intact specimens were subject to higher values of stress, in order to analyze the Low Cycle Fatigue (LCF) behavior, obtaining a Wöhler diagram for each type of specimen.

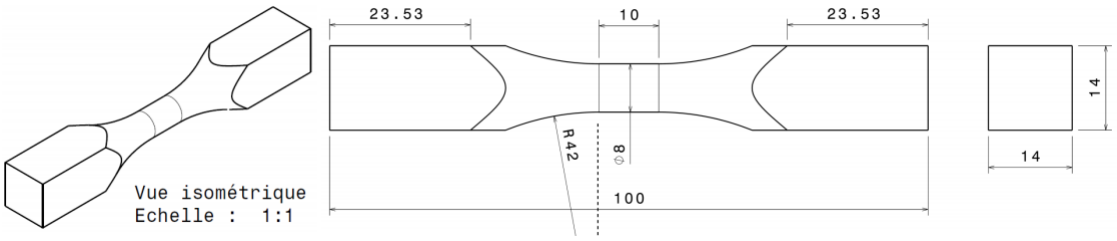

Figure 42: *Torsion specimen geometry*

3.2.4 Torsional fatigue tests

The geometry of the torsional specimens is detailed in figure 42. The tests were conducted on a resonant testing machine for tensile, bending and torsional tests: Rumul CRACKTRONIC®, displayed in figure 43.

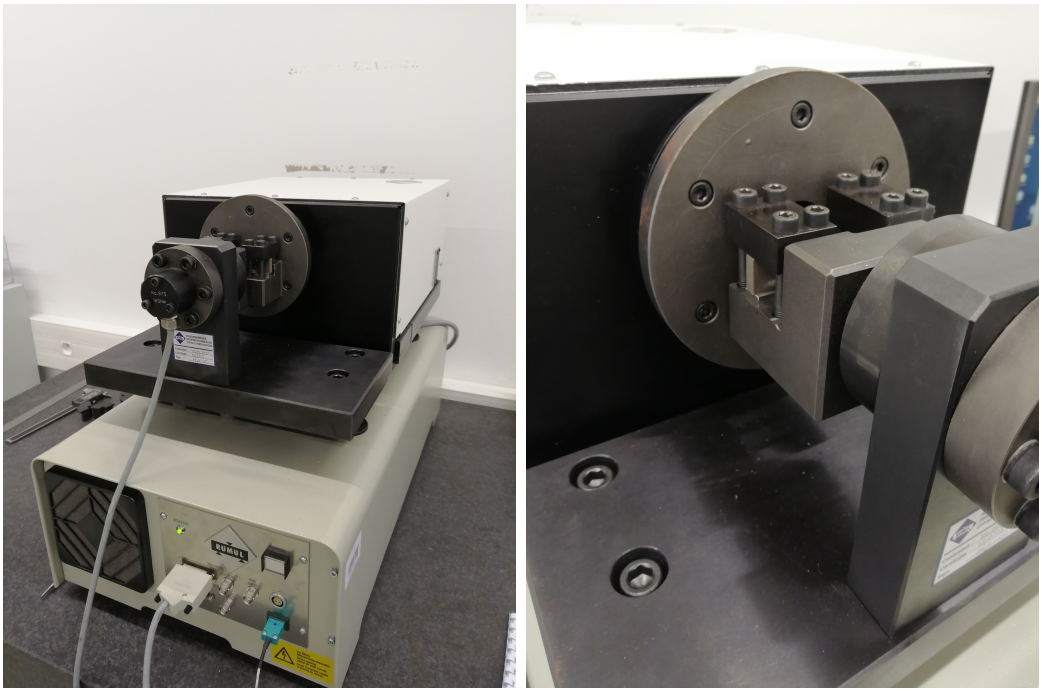

(a) General view (b) Detail on the specimen fixation

Figure 43: *Testing machine used for torsional and bending tests*

With this machine, the dynamic load is generated by a maintenance free oscillating system (resonator) oscillating in its natural frequency. The oscillating system consists of masses and springs, the specimen itself being part of this oscillating system. The machine works at resonance, thus a very high frequency can be achieved for the tests.

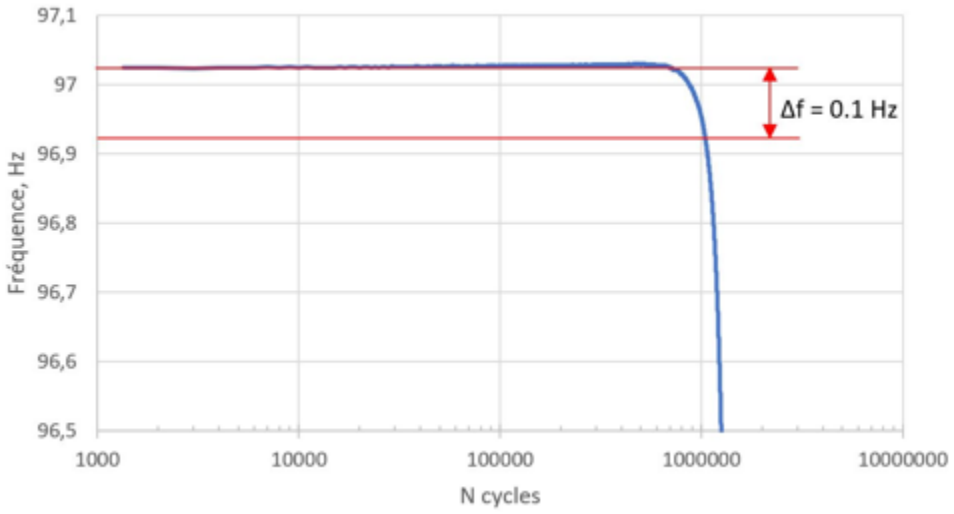

Figure 44: *Resonance frequency during a fatigue test*

A correspondingly controlled and excited electromagnet supplies as much energy to the oscillating system to reach and maintain the oscillating amplitude.
The frequency is then related to the specimen's rigidity, so the failure corresponds to a significant drop in frequency. For these tests the limit drop value, used to interrupt the test, was 0.5 Hz, but the failure was set in correspondence of a 0.1 Hz drop, represented in figure 44.
If at $2 \cdot 10^6$ cycles this drop had not been reached, the test was interrupted, with the intact sample.
As for the tensile tests, the staircase method was applied to set the torsional stress value; from this value, knowing the specimen diameter, the torque was calculated with:

$$M_t = \frac{2 \cdot \tau \cdot I_G}{d} \tag{13}$$

Where I_G is the second moment of area for a circular section:

$$I_G = \frac{\pi \cdot d^4}{32} \tag{14}$$

In this case, three staircases were conducted: one for the as-built specimens, one for the polished specimens, and one for the machined and polished specimens.
Again, as for the tensile tests, the intact specimens at the end of the staircases were tested at higher values of torsional stress, to obtain the Wöhler diagrams.

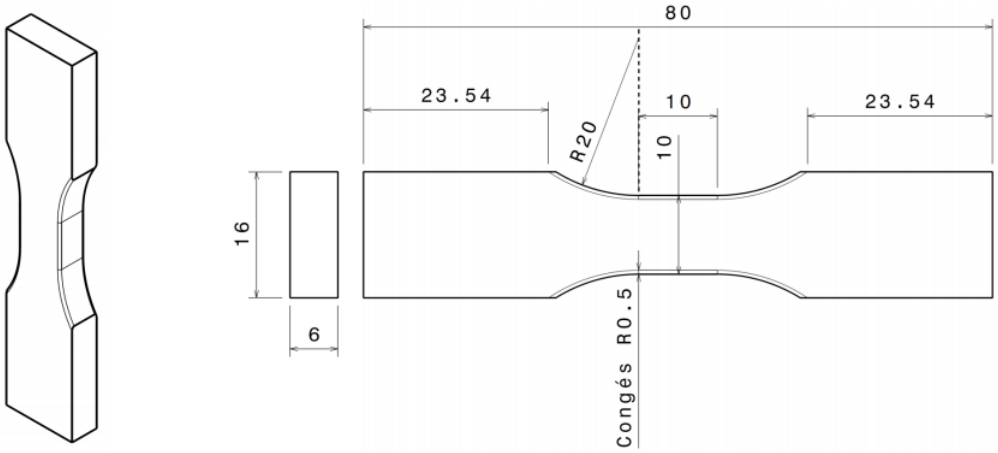

Figure 45: *Bending specimen geometry*

3.2.5 Bending fatigue tests

The geometry of the bending specimens is detailed in figure 45. The tests were conducted on the same resonant machine used for the torsional tests; again, the failure was considered for a frequency drop of 0.1 Hz, and the run-out was obtained at $2 \cdot 10^6$ cycles.
As for the tensile and the torsional tests, the staircase method was applied to set the stress value; from this value, knowing the specimen dimensions, the bending moment was calculated with:

$$M_b = \frac{\sigma \cdot J}{y} \tag{15}$$

Where J is the second moment of area for a rectangular section:

$$J = \frac{1}{12} b \cdot h^3 \tag{16}$$

And y is the perpendicular distance to the neutral axis:

$$y = \frac{h}{2} \tag{17}$$

With b and h the dimensions of the rectangular section. In this case, two different staircases were conducted: one for wrought, machined and polished specimens, one for SLM products machined and polished.
Moreover, in a previous study, two staircases were conducted [70]: one for as-built SLM products, and one for the polished ones.

3.3 Results and discussion

3.3.1 Tensile fatigue tests

The staircase method for the as-built and the polished specimens (**the ones from the tray 1 in blue, the ones from the tray 2 in red**) is shown in table 15.

Surface	Stress [MPa]	Test number									
-		1	2	3	4	5	6	7	8	9	10
As-built	100	X_{50}		X_{33}		X_{20}				X_{46}	
	90		O_{41}		O_{24}		X_{22}		O_{37}		
	80							O_9			
Polished	130	X_{12}									
	120		X_{25}		X_{39}		X_{35}		X_{19}		X_{15}
	110			O_{48}		O_{36}		O_3		O_{27}	

Table 15: *Staircase method for as-built and polished tensile specimens*

In the table, O_{xx} stands for run-out, while X_{xx} stands for failure. xx represents the specimen labeling number.
In both the cases, the run-outs are the least frequent events; the calculations for the parameters are shown in table 16.

Surface	i	f_i	$i \cdot f_i$	$i^2 \cdot f_i$
As-built	1	3	3	3
	0	1	0	0
	Σ	$F = 4$	$A = 3$	$B = 3$
Polished	0	4	0	0
	Σ	$F = 4$	$A = 0$	$B = 0$

Table 16: *Staircase method calculations for as-built and polished tensile specimens*

Finally, the endurance limit for the as-built samples is:

$$\sigma_D = \sigma_0 + d \cdot (\frac{A}{F} + \frac{1}{2}) = 80 + 10 \cdot (\frac{3}{4} + \frac{1}{2}) = 92.5MPa \tag{18}$$

In this case, the formula for the standard deviation is not valid, since the condition explained in (12) is not satisfied.
Instead, the endurance limit for the polished samples is:

$$\sigma_D = \sigma_0 + d \cdot (\frac{A}{F} + \frac{1}{2}) = 110 + 10 \cdot (\frac{0}{4} + \frac{1}{2}) = 115MPa \tag{19}$$

Also in this case, the formula for the standard deviation is not valid, since the condition explained in (12) is not satisfied.

As expected, the fatigue limit for the polished specimens was greater than the one for the as-built specimens, in particular with a 24% raise.
As already explained, the intact specimens were tested at higher stress values, as can be seen in table 17, and a Wöhler diagram, shown in figure 46, was developed for the two series of samples.
From this diagram, it is evident the better fatigue resistance for the polished specimens, even more clear at high stress values. It was supposed that this behavior is due to the elimination of some of the surface defects, the most superficial ones.

Surface	Specimen number	Stress [MPa]	Rupture cycles
As-built	26	120	711318
	50	100	1090413
	41	90	-
	33	100	1399298
	24	90	-
	20	100	1222525
	22	90	1588420
	9	80	-
	9	150	389131
	37	90	-
	37	130	563075
	46	100	1420531
	17	110	969382
	29	160	281144
Polished	12	130	866574
	25	120	1353541
	48	110	-
	48	150	725523
	39	120	950773
	36	110	-
	36	140	1062775
	35	120	1162360
	3	110	-
	19	120	1434796
	27	110	-
	15	120	1278695
	8	170	447987
	10	180	329954
	31	200	250285

Table 17: *Summary of all the tensile fatigue tests conducted*

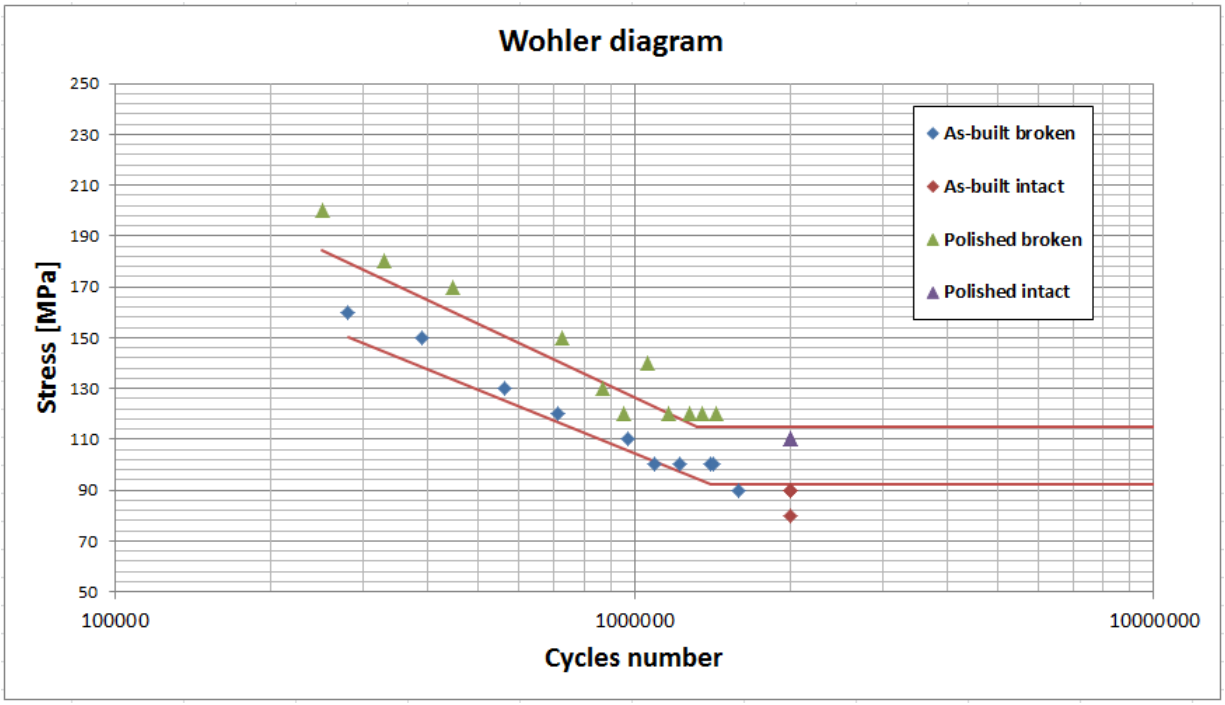

Figure 46: *Wöhler diagram for tensile specimens*

3.3.2 Torsional fatigue tests

The staircase method for the as-built, the polished and the machined and polished torsional specimens (**the ones from the tray 1 in blue, the ones from the tray 2 in red**) is shown in table 18.

Surface	Stress [MPa]	Test number												
-		1	2	3	4	5	6	7	8	9	10	11	12	13
As-built	140										X_{13}		X_7	
	130	X_{11}		X_{24}				X_{15}		O_{25}		O_6		X_{23}
	120		O_{20}		X_4		O_{27}		O_8					
	110					O_5								
Polished	150	X_{16}				X_5		X_6		X_{25}				
	140		X_{22}		O_{18}		O_{27}		O_{10}		O_2			
	130			O_{30}										
Machined & Polished	180			X_{29}				X_{10}		X_{28}				
	170		O_{14}		X_1		O_2		O_{18}		O_{30}			
	160	O_3				O_{21}								

Table 18: *Staircase method for as-built, polished, machined and polished torsional specimens*

For the as-built specimens, the run-outs are the least frequent events; for the polished ones, the run-outs and the failures are equally frequent; for the machined and polished ones, the failures are the less frequent events; the calculations for the parameters are shown in table 19.

Surface	i	f_i	$i \cdot f_i$	$i^2 \cdot f_i$
As-built	2	2	4	8
	1	3	3	3
	0	1	0	0
	Σ	$F = 6$	$A = 7$	$B = 11$
Polished	1	4	4	4
	0	1	0	0
	Σ	$F = 5$	$A = 4$	$B = 4$
Machined & Polished	1	3	3	3
	0	1	0	0
	Σ	$F = 4$	$A = 3$	$B = 3$

Table 19: *Staircase method calculations for as-built, polished, machined and polished torsional specimens*

Finally, the endurance limit for the as-built specimens is:

$$\tau_D = \tau_0 + d \cdot (\frac{A}{F} + \frac{1}{2}) = 110 + 10 \cdot (\frac{7}{6} + \frac{1}{2}) = 126.67MPa \tag{20}$$

In this case, the condition for the validity of the standard deviation formula is satisfied; thus:

$$s = 1.62 \cdot d \cdot (\frac{F \cdot B - A^2}{F^2} + 0.029) = 8.12MPa \tag{21}$$

Instead, the endurance limit for the polished specimens is:

$$\tau_D = \tau_0 + d \cdot (\frac{A}{F} + \frac{1}{2}) = 130 + 10 \cdot (\frac{4}{5} + \frac{1}{2}) = 143MPa \tag{22}$$

In this case, the formula for the standard deviation is not valid, since the condition explained in (12) is not satisfied.
Finally, the endurance limit for machined and polished specimens is:

$$\tau_D = \tau_0 + d \cdot (\frac{A}{F} - \frac{1}{2}) = 170 + 10 \cdot (\frac{3}{4} - \frac{1}{2}) = 172.5MPa \tag{23}$$

In this case, the formula for the standard deviation is not valid, since the condition explained in (12) is not satisfied.

Again, the fatigue limit is increased when the surface is polished (13% raise), and even more when the surface is machined and polished (36% raise). Nevertheless, the improvement is less significant than the one obtained for the traction.
As for the traction, the intact specimens were tested at higher stress values, as can be seen in table 20, and a Wöhler diagram, shown in figure 47 was developed for the three series of samples.

Surface	Specimen number	Stress [MPa]	Rupture cycles
As-built	7 (tray 1)	150	634502
	11 (tray 1)	130	1686003
	20 (tray 1)	120	-
	20 (tray 1)	180	263201
	24 (tray 2)	130	1405000
	4 (tray 2)	120	1661001
	5 (tray 2)	110	-
	5 (tray 2)	150	858506
	27 (tray 2)	120	-
	15 (tray 2)	130	1993002
	8 (tray 2)	120	-
	8 (tray 2)	170	793004
	25 (tray 2)	130	-
	25 (tray 2)	160	851003
	13 (tray 2)	140	849507
	6 (tray 2)	130	-
	6 (tray 2)	200	283004
	7 (tray 2)	140	992000
	23 (tray 2)	130	1112505
Polished	3	180	568007
	1	170	668503
	16	150	1328000
	22	140	1246500
	30	130	-
	30	160	776003
	18	140	-
	18	200	290203
	5	150	843505
	27	140	-
	27	210	262257
	6	150	1298005
	10	140	-
	10	190	461006
	25	150	1285002
	2	140	-

	18	200	290203
	3	160	-
	3	220	649754
	14	170	-
	14	190	773005
	29	180	1669000
	1	170	873004
Machined	21	160	-
&	2	170	-
Polished	2	240	360444
	10	180	1563000
	18	170	-
	18	200	1216004
	28	180	705173
	30	170	-
	30	250	157506

Table 20: *Summary of all the torsional fatigue tests conducted*

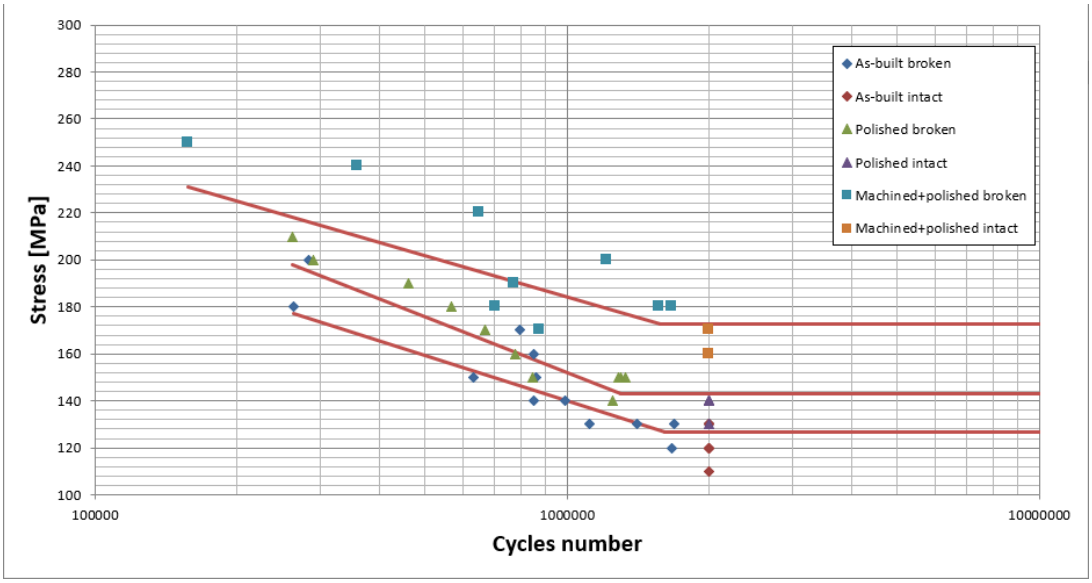

Figure 47: *Wöhler diagram for torsional specimens*

As for the tensile tests, this diagram shows the better fatigue resistance for the polished specimens, even more clear at high stress values, and in addition it shows a significant improvement for the machined and polished specimens. This is supposedly due to the fact that the machining and polishing eliminates more surface defects than the simple polishing.

3.3.3 Bending fatigue tests

The staircase method for the as-built, the polished and the machined and polished bending specimens (**the ones from the tray 1 in blue, the ones from the tray 2 in red**) is shown in table 21. The data for the as-built and the polished specimens are taken from [70].

Surface	Stress [MPa]	Test number													
-		1	2	3	4	5	6	7	8	9	10	11	12	13	14
As-built	100	X_1				X_{12}		X_7						X_8	
	90		X_{28}		O_{25}		O_4		X_{29}		X_{17}		O_{18}		X_{30}
	80			O_{22}						O_2		O_{19}			
Polished	130		X_{23}		X_{16}										
	120	O_5		O_{21}		X_{11}				X_9		X_{24}		X_{20}	
	110						X_{27}		O_6		O_3		O_{13}		O_{15}
	100							O_{26}							
Machined & Polished	150							X_3							
	140		X_4		X_{26}		O_2		X_6						
	130	O_{22}		O_{13}		O_{10}				O_{28}					

Table 21: *Staircase method for as-built, polished, machined and polished bending specimens*

For the three cases, the failures were the least frequent events; the calculations for the parameters are shown in table 22.

Surface	i	f_i	$i \cdot f_i$	$i^2 \cdot f_i$
As-built	1	3	3	3
	0	3	0	0
	Σ	$F = 6$	$A = 3$	$B = 3$
Polished	2	2	4	8
	1	4	4	4
	0	1	0	0
	Σ	$F = 7$	$A = 8$	$B = 12$
Machined & Polished	1	1	1	1
	0	3	0	0
	Σ	$F = 4$	$A = 1$	$B = 1$

Table 22: *Staircase method calculations for as-built, polished, machined and polished bending specimens*

Finally, the endurance limit for the machined and polished specimens is:

$$\sigma_D = \sigma_0 + d \cdot (\frac{A}{F} - \frac{1}{2}) = 140 + 10 \cdot (\frac{1}{4} - \frac{1}{2}) = 137.5MPa \tag{24}$$

Stress [MPa]	Test number									
-	1	2	3	4	5	6	7	8	9	10
300					X_6				X_{10}	
290				O_5		X_7		O_9		O_{11}
280	X_2		O_4				O_8			
270		O_3								

Table 23: *Staircase method for wrought, machined and polished bending specimens*

i	f_i	$i \cdot f_i$	$i^2 \cdot f_i$
2	2	4	8
1	1	1	1
0	1	0	0
Σ	$F = 4$	$A = 5$	$F = 9$

Table 24: *Staircase method calculations for wrought, machined and polished bending specimens*

In this case, the formula for the standard deviation is not valid, since the condition explained in (12) is not satisfied.
The endurance limits for the as-built and polished specimens were, respectively:

$$\sigma_D = 90MPa \tag{25}$$

$$\sigma_D = 116.4MPa \tag{26}$$

As already explained, for the bending specimens also a staircase for the wrought, machined and polished ones was conducted. The tests are shown in table 23.
In this case, the failures are the least frequent events; the calculations for the parameters are shown in table 24.
Finally, the endurance limit is:

$$\sigma_D = \sigma_0 + d \cdot (\frac{A}{F} - \frac{1}{2}) = 280 + 10 \cdot (\frac{5}{4} - \frac{1}{2}) = 287.5MPa \tag{27}$$

In this case, the condition for the validity of the standard deviation formula is satisfied; thus:

$$s = 1.62 \cdot d \cdot (\frac{F \cdot B - A^2}{F^2} + 0.029) = 11.61MPa \tag{28}$$

As for the other tests, the fatigue limit is raised when the surface is polished (29% raise), and even more when the surface is machined and polished (53% raise). Nevertheless, these values are significantly smaller than the one obtained for the wrought, machined and polished specimens.

Again, the intact specimens were tested at higher stress values as can be seen in tables 25, 26, and a Wöhler diagram, shown in figure 48, was developed for the four series of samples, considering also the data from the previous project [70].

Surface	Specimen number	Stress [MPa]	Rupture cycles
As-built [70]	22	80	-
	2	80	-
	19	80	-
	29	90	2575000
	30	90	1737000
	28	90	1849000
	17	90	2055000
	25	90	-
	4	90	-
	18	90	-
	1	100	1047000
	12	100	1511000
	7	100	2055000
	8	100	2204000
	25	110	730000
	19	120	375000
	18	140	189000
	2	160	110000
	4	170	100000
Polished [70]	26	100	-
	27	110	1525000
	6	110	-
	3	110	-
	13	110	-
	15	110	-
	5	120	-
	21	120	-
	11	120	1600000
	9	120	1357000
	24	120	1587000
	20	120	1139000
	23	130	888000
	16	130	911000
	21	140	580000
	15	150	548000
	13	170	319000
	3	190	204000
	6	210	140000

	26	230	100000
Machined & Polished	22	130	-
	22	160	567501
	4	140	1205008
	13	130	-
	13	170	508001
	26	140	1144001
	10	130	-
	10	150	724004
	2	140	-
	2	180	372001
	3	150	784305
	6	140	1622504
	28	130	-
	28	200	314301

Table 25: *Summary of all the bending fatigue tests conducted*

Specimen number	Stress [MPa]	Rupture cycles
3	300	671206
4	320	750008
5	360	207758
8	340	413006
9	310	712007
10	330	778609
11	350	370001

Table 26: *LCF tests on wrought, machined and polished bending specimens*

As for the other tests, this diagram shows a first improvement in fatigue resistance when the surface is polished, and a second one when the surface is machined and polished.
Nevertheless, when compared with the values obtained for wrought, machined and polished values, the results from SLM products are significantly worse.

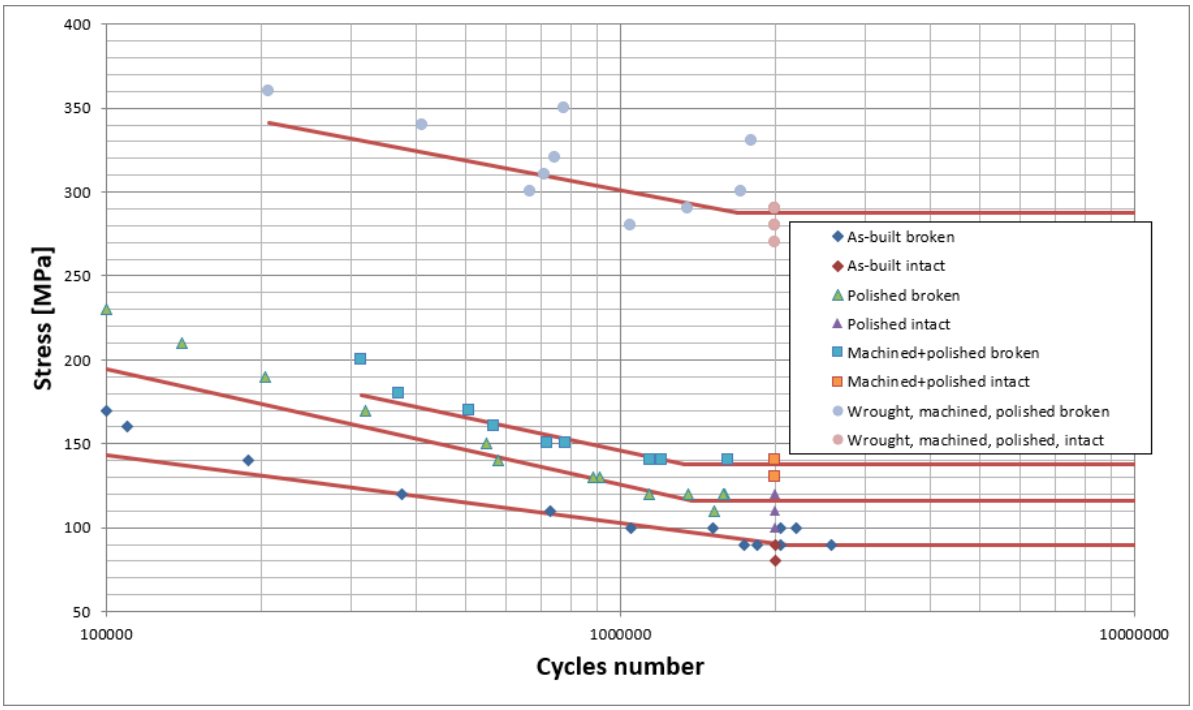

Figure 48: *Wöhler diagram for bending specimens*

3.4 Conclusion

In this part of the project the fatigue behavior of the stainless steel 316L produced by SLM was analyzed.
It was observed that this technique produces parts with quite high roughness, and some lack-of fusion defects. These two aspects can negatively influence the fatigue resistance of a part, providing micro-cracks (on the surface and internally), that can start propagating when a stress is applied.
The solutions to eliminate the presence of the micro-cracks consist of surface treatments, to decrease the roughness, and heat treatments, for the internal defects.
In this project, the tested samples had received three different types of surface treatments: some specimens were tested in as-built conditions, others were polished, and finally others were machined, in order to eliminate 0.25 mm from the surface, and then polished.
All the conducted tests (tensile, torsional and bending) provided the same result: a first improvement in fatigue resistance for the polished samples, and a second, more significant, improvement for the machined and polished samples. Nevertheless, a comparison with wrought, machined and polished specimens showed that the fatigue resistance is worse for SLM products.

4 Conclusion and perspectives

Additive Manufacturing techniques are quickly developing in these years, as they can provide advantages especially in terms of time, scrap and weight reduction. Among these techniques, Selective Laser Melting has turned out to be one of the most popular, especially for the titanium alloy Ti6Al4V and the stainless steel 316L, two very important materials in the aeronautical sector.
Two important observations can be made about SLM: it was observed that its products show an anisotropic behavior, caused by an anisotropic microstructure and the presence of defects, and also it was observed that the fatigue resistance is quite low, due to the high roughness and the presence of internal defects.
In this project some tests have been conducted, to study the anisotropic behavior of Ti6Al4V and the fatigue resistance of SS316L.
For the first part, a significant anisotropy was observed for the elongation at rupture, and a less significant one was observed for the strength. The best results were provided by samples whose build direction was parallel to the principal stress direction. Nevertheless, the strength results are in general better than the reference values for wrought, annealed parts, while the ductility is lower.
For the second part, an improvement in fatigue resistance was observed when the surface of the tested samples was polished, and an even better improvement when the surface was machined and polished. However, in comparison to the results obtained for wrought samples, all the SLM specimens showed a worse resistance. These results are consistent with the consulted articles, and show that SLM is a promising technique, but it still has some disadvantages when compared to more traditional techniques.

References

[1] B. Dutta, F.H. Froes, *The Additive Manufacturing (AM) of titanium alloys*, Metal Powder Report, Volume 72, Issue 2, Pages 96-106 (2017)

[2] I. Inagaki, T. Takechi, Y. Shirai, N. Ariyasu, *Application and Features of Titanium for the Aerospace Industry*, Nippon Steel & Sumitomo Metal Technical Report Number 106 (2014)

[3] M. Peters, J. Kumpfert, C.H. Ward, C. Leyens, *Titanium Alloys for Aerospace Applications*, Titanium and Titanium Alloys, Pages 333-350 (2001)

[4] B. Dutta, F. H. Froes, *Additive Manufacturing of Titanium Alloys: State of the Art, Challenges and Opportunities*, Butterworth-Heinemann, Pages 1-10 (2016)

[5] W. Boas, J.K. Mackenzie, *Anisotropy in Metals*, Progress in Metal Physics, Volume 2, Pages 90-120 (1950)

[6] B. Hutchinson, *Critical Assessment 16: Anisotropy in metals*, Materials Science and Technology, 31:12, Pages 1393-1401 (2015)

[7] ASTM F2792-12a, *Standard Terminology for Additive Manufacturing Technologies*, ASTM International, West Conshohocken, PA, 2012, `www.astm.org`

[8] T. Wohlers, *Wohlers Report*, Wohlers Associates (2018)

[9] D. Herzog, V. Seyda, E. Wycisk, C. Emmelmann, *Additive manufacturing of metals*, Acta Materialia 117, Pages 371-392 (2016)

[10] W. Meiners, K. Wissenbach, A. Gasser, *Shaped body especially prototype or replacement part production*, DE19649865C1 (1996)

[11] C. Li, Z.Y. Liu, X.Y. Fang, Y.B. Guo, *Residual Stress in Metal Additive Manufacturing*, CIRP Annals, Volume 71, Issue 1, Pages 348-353 (2018)

[12] M. Shiomi, K. Osakada, K. Nakamura, T. Yamashita, F. Abe, *Residual Stress within Metallic Model Made by Selective Laser Melting Process*, CIRP Annals, Volume 53, Issue 1, Pages 195-198 (2004)

[13] C.Y. Yap, C.K. Chua, Z.L. Dong, Z.H. Liu, D.Q. Zhang, L.E. Loh, S.L. Sing, *Review of selective laser melting: Materials and applications*, Applied Physics Reviews 2, 041101 (2015)

[14] D. Sun, D. Gu, K. Lin, J. Ma, W. Chen, J. Huang, X. Sun, M. Chu, *Selective laser melting of titanium parts: Influence of laser process parameters on macro- and microstructures and tensile property*, Powder Technology, Volume 342, Pages 371-379 (2019)

[15] B. Vandenbroucke, J.P. Kruth, *Selective laser melting of biocompatible metals for rapid manufacturing of medical parts*, Rapid Prototyping Journal, Vol. 13 Issue: 4, Pages 196-203 (2007)

[16] R. Boyer, G. Welsch, E. W. Collings, *Materials Properties Handbook: Titanium Alloys*, ASM International, Materials Park, OH, USA (1994)

[17] P.Krakhmalev, G.Fredriksson, I.Yadroitsava, N.Kazantseva, A. du Plessis, I.Yadroitsev, *Deformation Behavior and Microstructure of Ti6Al4V Manufactured by SLM*, Physics Procedia, Volume 83, Pages 778-788 (2016)

[18] M. Simonelli, Y, Y. Tse, C. Tuck, *On the Texture Formation of Selective Laser Melted Ti-6Al-4V*, Metallurgical and Materials Transactions A, Volume 45, Issue 6, Pages 2863–2872 (2014)

[19] L. Thijs, F. Verhaeghe, T. Craeghs, J. Van Humbeeck, J. P. Kruth, *A study of the microstructural evolution during selective laser melting of Ti–6Al–4V*, Acta Materialia, Volume 58, Pages 3303-3312 (2010)

[20] B. E. Carroll, T. A. Palmera, A. M. Beese, *Anisotropic tensile behavior of Ti–6Al–4V components fabricated with directed energy deposition additive manufacturing*, Acta Materialia, Volume 87, Pages 309–320 (2015)

[21] N. Hrabe, T. Quinn, *Effects of processing on microstructure and mechanical properties of a titanium alloy (Ti–6Al–4V) fabricated using electron beam melting (EBM), Part 2: Energy input, orientation, and location*, Materials Science and Engineering: A, Volume 573, Pages 271-277 (2013)

[22] P. Edwards, A. O'Conner, M. Ramulu, *Electron Beam Additive Manufacturing of Titanium Components: Properties and Performance*, Journal of Manufacturing Science and Engineering, Volume 135, Issue 6 (2013)

[23] N. Hrabe, T. Quinn, *Effects of processing on microstructure and mechanical properties of a titanium alloy (Ti–6Al–4V) fabricated using electron beam melting (EBM), Part 1: Distance from build plate and part size*, Materials Science and Engineering: A, Volume 573, Pages 264-270 (2013)

[24] B. Vrancken, L. Thijs, J. P. Kruth, J. Van Humbeeck, *Heat treatment of Ti6Al4V produced by Selective Laser Melting: Microstructure and mechanical properties*, Journal of Alloys and Compounds 541, Pages 177–185 (2012)

[25] H.K. Rafi, N.V. Karthik, H. Gong, T. L. Starr, B. E. Stucker, *Microstructures and Mechanical Properties of Ti6Al4V Parts Fabricated by Selective Laser Melting and Electron Beam Melting*, Journal of Materials Engineering and Performance, Volume 22, Issue 12, Pages 3872–3883 (2013)

[26] T. Vilaro, C. Colin, J.D. Bartout, *As-Fabricated and Heat-Treated Microstructures of the Ti-6Al-4V Alloy Processed by Selective Laser Melting*, Met-

allurgical and Materials Transactions A, Volume 42, Issue 10, Pages 3190–3199 (2011)

[27] L. Facchini, E. Magalini, P. Robotti, A. Molinari, S. Höges, K. Wissenbach, *Ductility of a Ti-6Al-4V alloy produced by selective laser melting of prealloyed powders*, Rapid Prototyping Journal, Volume 16, Issue 6, Pages 450-459 (2010)

[28] P. A. Kobryn, S. L. Semiatin, *Mechanical properties of laser-deposited Ti-6Al-4V*, Solid Freeform Fabrication Proceedings, The University of Texas: Austin, TX, USA (2001)

[29] P. A. Kobryn, E. H. Moore, S. L. Semiatin, *The effect of laser power and traverse speed on microstructure, porosity, and build height in laser-deposited Ti-6Al-4V*, Scripta Materialia, Volume 43, Issue 4, Pages 299-305 (2000)

[30] B. E. Carroll, T. A. Palmer, A. M.Beese, *Anisotropic tensile behavior of Ti–6Al–4V components fabricated with directed energy deposition additive manufacturing*, Acta Materialia, Volume 87, Pages 309-320 (2015)

[31] D. A. Hollander, M. von Walter, T. Wirtz, R. Sellei, B. Schmidt-Rohlfing, O. Paar, H. J. Erli, *Structural, mechanical and in vitro characterization of individually structured Ti–6Al–4V produced by direct laser forming*, Biomaterials, Volume 27, Issue 7, Pages 955-963 (2006)

[32] S. Leuders, M. Thöne, A. Riemer, T. Niendorf, T. Tröster, H. A. Richard, H. J. Maier, *On the mechanical behaviour of titanium alloy TiAl6V4 manufactured by selective laser melting: Fatigue resistance and crack growth performance*, International Journal of Fatigue, Volume 48, Pages 300-307 (2013)

[33] M. J. Donachie, *Titanium: A Technical Guide, 2nd edition*, ASM International, Materials Park, OH, USA (2000)

[34] B. Baufeld, E. Brandl, O. van der Biest, *Wire based additive layer manufacturing: Comparison of microstructure and mechanical properties of Ti–6Al–4V components fabricated by laser-beam deposition and shaped metal deposition*, Journal of Materials Processing Technology, Volume 211, Issue 6, Pages 1146-1158 (2011)

[35] D. Agius, K. I. Kourousis, C. Wallbrink, T. Song, *Cyclic plasticity and microstructure of as-built SLM Ti-6Al-4V: The effect of build orientation*, Materials Science and Engineering: A, Volume 701, Pages 85-100 (2017)

[36] J. Alcisto, A. Enriquez, H. Garcia, S. Hinkson, T. Steelman, E. Silverman, P. Valdovino, H. Gigerenzer, J. Foyos, J. Ogren, J. Dorey, K. Karg, T. McDonald, O. S. Es-Said, *Tensile Properties and Microstructures of Laser-Formed Ti-6Al-4V*, Journal of Materials Engineering and Performance, Volume 20, Issue 2, Pages 203-212 (2011)

[37] J. Yang, H. Yu, Z. Wang, X. Zeng, *Effect of crystallographic orientation on mechanical anisotropy of selective laser melted Ti-6Al-4V alloy*, Materials Characterization, Volume 127, Pages 137-145 (2017)

[38] M. Simonelli, Y. Y. Tse, C. Tuck, *Effect of the build orientation on the mechanical properties and fracture modes of SLM Ti–6Al–4V*, Materials Science and Engineering: A, Volume 616, Pages 1-11 (2014)

[39] D. Banerjee, J.C. Williams, *Perspectives on titanium science and technology*, Acta Materialia, Volume 61, Pages 844-879 (2013)

[40] H. Gong, K. Rafi, H. Gu, G. D. Janaki Ram, T. Starr, B. Stucker, *Influence of defects on mechanical properties of Ti–6Al–4 V components produced by selective laser melting and electron beam melting*, Materials and Design, Volume 86, Pages 545-554 (2015)

[41] D. Jia, Y. M. Wang, K.T. Ramesh, E. Ma, Y. T. Zhu, R. Z. Valiev, *Deformation behavior and plastic instabilities of ultrafine-grained titanium*, Applied Physics Letters, Volume 79, Issue 5, Pages 611-613 (2001)

[42] Y. Kok, X. P. Tan, P. Wang, M. L. S. Nai, N. H. Loh, E. Liu, S. B. Tor, *Anisotropy and heterogeneity of microstructure and mechanical properties in metal additive manufacturing: A critical review*, Materials and Design, Volume 139, Pages 565-586 (2018)

[43] ASTM B831-14, *Standard Test Method for Shear Testing of Thin Aluminum Alloy Products*, ASTM International, West Conshohocken, PA, 2014, `www.astm.org`

[44] Q. Yin, B. Zillmann, S. Suttner, G. Gerstein, M. Biasutti, A. E. Tekkaya, M. F. X. Wagner, M. Merklein, M. Schaper, T. Halle, A. Brosius, *An experimental and numerical investigation of different shear test configurations for sheet metal characterization*, International Journal of Solids and Structures, Volume 51, Pages 1066-1074 (2014)

[45] A. Öchsner, *Continuum Mechanics of Plasticity*, Elasto-plasticity of frame structure elements: Modeling and simulation of rods and beams, Pages 5-35 (2014)

[46] S. Shrivastava, C. Ghosh, J. J. Jonas, *A comparison of the von Mises and Hencky equivalent strains for use in simple shear experiments*, Philosophical Magazine, Volume 92, Number 7, Pages 779-786 (2011)

[47] Y. Zhong, L. E. Rännar, L. Liu, A. Koptyug, S. Wikman, J. Olsén, D. Cui, Z. Shen, *Additive manufacturing of 316L stainless steel by electron beam melting for nuclear fusion applications*, Journal of Nuclear Materials, Volume 486, Pages 234-245 (2017)

[48] ASM International Handbook Committee, *Materials Handbook*, Edition 10, Volume 1, ASM International, Materials Park, OH, USA (1990)

[49] C. Bathias, P. C. Paris, *Gigacycle fatigue in mechanical practice*, Edition 1, Marcel Dekker, New York, NY, USA (2005)

[50] Q. Xin, *Durability and reliability in diesel engine sistem design*, Diesel Engine System Design, (2013)

[51] N. Shamsaei, J. Simsiriwong, *Fatigue behaviour of additively-manufactured metallic parts*, Procedia Structural Integrity, Volume 7, Pages 3-10 (2017)

[52] H. Masuo, Y. Tanaka, S. Morokoshi, H. Yagura, T. Uchida, Y. Yamamoto, Y. Murakami, *Effects of Defects, Surface Roughness and HIP on Fatigue Strength of Ti-6Al-4V manufactured by Additive Manufacturing*, Procedia Structural Integrity, Volume 7, Pages 19-26 (2017)

[53] T. M. Mower, M. J. Long, *Mechanical behavior of additive manufactured, powder-bed laser-fused materials*, Materials Science and Engineering: A, Volume 651, Pages 198-213 (2016)

[54] Y. Xue, A. Pascu, M. F. Horstemeyer, L. Wang, P. T. Wang, *Microporosity effects on cyclic plasticity and fatigue of LENS™-processed steel*, Acta Materialia, Volume 58, Issue 11, Pages 4029-4038 (2010)

[55] A. Falkowska, A. Seweryn, A. Tomczyk, *Fatigue life and strength of 316L sintered steel of varying porosity*, International Journal of Fatigue, Volume 111, Pages 161-176 (2018)

[56] N. P. Lavery, J. Cherry, S. Mehmood, H. Davies, B. Girling, E. Sackett, S. G. R. Brown, J. Sienz, *Effects of hot isostatic pressing on the elastic modulus and tensile properties of 316L parts made by powder bed laser fusion*, Materials Science and Engineering: A, Volume 693, Pages 186-213 (2017)

[57] P. Edwards, M. Ramulu, *Fatigue performance evaluation of selective laser melted Ti–6Al–4V*, Materials Science and Engineering: A, Volume 598, Pages 327-337 (2014)

[58] H. V. Atkinson, S. Davies, *Fundamental aspects of hot isostatic pressing: An overview*, Metallurgical and Materials Transactions A, Volume 31, Issue 12, Pages 2981–3000 (2000)

[59] K. Kempen, L. Thijs, E. Yasa, M. Badrossamay, W. Verheecke, J. P. Kruth, *Process Optimization and Microstructural Analysis for Selective Laser Melting of AlSi10Mg*, 22nd Annual International Solid Freeform Fabrication Symposium (2011)

[60] A. Safdar, H .Z. He, L. Y. Wei, A. Snis, L. E. Chavez de Paz, *Effect of process parameters settings and thickness on surface roughness of EBM produced Ti-6Al-4V*, Rapid Prototyping Journal, Volume 18, Issue 5, Pages 401-408 (2012)

[61] R. J. Moat, A. J. Pinkerton, L. Li, P. J. Withers, M. Preuss, *Residual stresses in laser direct metal deposited Waspaloy*, Materials Science and Engineering: A, Volume 528, Issue 6, Pages 2288-2298 (2011)

[62] G. Bussu, P. E. Irving, *The role of residual stress and heat affected zone properties on fatigue crack propagation in friction stir welded 2024-T351 aluminium joints*, International Journal of Fatigue, Volume 25, Issue 1, Pages 77-88 (2003)

[63] P. Rangaswamy, M. L. Griffith, M. B. Prime, T. M. Holden, R. B. Rogge, J. M. Edwards, R. J. Sebring, *Residual stresses in LENS® components using neutron diffraction and contour method*, Materials Science and Engineering: A, Volume 399, Issues 1-2, Pages 72-83 (2005)

[64] R. I. Stephens, A. Fatemi, R. R. Stephens, H. O. Fuchs, *Metal fatigue in engineering*, Edition 2, John Wiley & Sons Ltd, New York, NY, USA (2000)

[65] S. Leuders, T. Lieneke, S. Lammers, T. Tröster, T. Niendorf, *On the fatigue properties of metals manufactured by selective laser melting – The role of ductility*, Journal of Materials Research, Volume 29, Issue 1911-1919, Pages 72-83 (2014)

[66] A. Riemer, S. Leuders, M. Thöne, H. A. Richard, T. Tröster, T. Niendorf, *On the fatigue crack growth behavior in 316L stainless steel manufactured by selective laser melting*, Engineering Fracture Mechanics, Volume 120, Pages 15-25 (2014)

[67] E. S. Puchi-Cabrera, F. Matınez, I. Herrera, J. A. Berrıos, S. Dixit, D. Bhat, *On the fatigue behavior of an AISI 316L stainless steel coated with a PVD TiN deposit*, Surface and Coatings Technology, Volume 182, Pages 276-286 (2004)

[68] A. B. Spierings, T. L. Starr, K. Wegener, *Fatigue performance of additive manufactured metallic parts*, Rapid Prototyping Journal, Volume 19, Issue 2, Pages 88-94 (2013)

[69] W. J. Dixon, A. M. Mood, *A Method for Obtaining and Analyzing Sensitive Data*, Journal of the American Statistical Association, Volume 43, Pages 109-126 (2013)

[70] N. Dorofeev, *La tenue en fatigue de l'acier 316L élaboré par fabrication additive*, ISAE Supaero (2018)